ATLAS PUB Note
ATL-PHYS-PUB-2018-051
17th December 2018

Prospects for jet and photon physics at the HL-LHC and HE-LHC

The ATLAS Collaboration

In this note prospects for the measurement of the inclusive jet, dijet, inclusive prompt photon and photon+jet production cross sections in proton-proton collisions at 14 and 27 TeV are presented. Double differential predictions for the inclusive jet cross sections as a function of the absolute jet rapidity and jet transverse momentum and the dijet spectrum as a function of half the absolute rapidity separation between the two highest transverse momentum jets and the invariant mass of these two jets are evaluated. Relevant uncertainties, including the individual contributions to the jet energy scale uncertainty, are calculated for jets with $p_{\mathrm{T}} > 100$ GeV within jet rapidity $|y| < 3$. Expectations for inclusive isolated photons are presented in terms of cross sections differentially in photon transverse energy in different ranges of photon pseudorapidity. Estimations for photon+jet events are described in terms of distributions in photon transverse energy, jet transverse momentum, invariant mass of the photon+jet system and $|\cos\theta^*|$. The study covers the region of photon transverse energies above 400 GeV and jet transverse momenta in excess of 300 GeV. A good understanding of these processes is of relevance for searches for new phenomena beyond the Standard Model. The sensitivity of these processes to the parton distribution functions in the proton is also shown.

ATL-PHYS-PUB-2018-051
19 December 2018

© 2018 CERN for the benefit of the ATLAS Collaboration.
Reproduction of this article or parts of it is allowed as specified in the CC-BY-4.0 license.

1 Introduction

Precise measurements of jet and photon production cross sections are crucial in understanding physics at hadron colliders. Inclusive jet production ($p + p \rightarrow \text{jet} + X$) cross sections, dijet production ($p + p \rightarrow \text{jet} + \text{jet} + X$) cross sections as well as inclusive photon production ($p + p \rightarrow \gamma + X$) cross sections and cross sections for associated photon and jet production ($p + p \rightarrow \gamma + \text{jet} + X$) provide valuable information about the strong coupling constant (α_s) and the parton density functions (PDFs) of the proton. Furthermore, events with jets and photons in the final-state represent a background to many other processes at the Large Hadron Collider (LHC) [1]. A good understanding of the photon and jet production processes is therefore relevant in many searches for new physics.

The LHC provided pp collisions at centre-of-mass energies $\sqrt{s} = 7, 8$ and 13 TeV and delivered more than 385 fb^{-1} to the ALICE, ATLAS, CMS and LHCb experiments during the Run-1 and Run-2 data-taking periods. The high-luminosity phase of the Large Hadron Collider (HL-LHC) is expected to start in 2026 with pp collisions at $\sqrt{s} = 14$ TeV and will deliver a total integrated luminosity of about 6000 fb^{-1} to all experiments. The High-Energy LHC (HE-LHC) is expected to use the existing LHC tunnel and provide pp collisions at $\sqrt{s} = 27$ TeV to collect more than 15000 fb^{-1} of data over 20 years of operation.

Production of jets and photons in pp collisions are among the processes directly testing the smallest experimentally accessible space-time distances. Next-to-leading-order (NLO) perturbative QCD calculations [2, 3] give quantitative predictions of the jet production cross sections. Progress in next-to-next-to-leading-order (NNLO) QCD calculations has been made recently [4–6]. As fixed-order QCD calculations only make predictions for the quarks and gluons associated with the short-distance scattering process, corrections for the fragmentation of these partons to particles need to be evaluated.

The production of prompt photons inclusively and in association with at least one jet in pp collisions provides a testing ground for perturbative QCD with a hard colourless probe. All photons produced in pp collisions that are not from hadron decays are considered as "prompt". Two processes contribute to prompt-photon production: the direct process, in which the photon originates directly from the hard interaction, and the fragmentation process, in which the photon is emitted in the fragmentation of a high transverse momentum parton [7, 8].

Measurements of the cross sections for inclusive isolated-photon production and associated photon and jet production at the highest photon transverse energies (E_{T}^{γ}) and jet transverse momenta ($p_{\text{T}}^{\text{jet}}$) as well as jet production at highest jet transverse momentum and dijet invariant mass allow for tests of the Standard Model predictions in a regime beyond what has been explored so far. They represent a wealth of data to test the fixed order calculations as well as investigate novel approaches to the description of parton radiation and evaluate the importance of electroweak corrections in pure QCD production processes calculations. In addition, since the dominant photon production mechanism in pp collisions at the LHC proceeds via the $qg \rightarrow q\gamma$ channel and the jet production goes via gg and qg scatterings (with qq channel providing a large contribution in the high-p_{T} range), those measurements are sensitive to the gluon density in the proton [9–12]. Furthermore, those measurements validate the modelling used for background studies in searches for physics beyond the Standard Model that involve photons and jets, such as the search for new phenomena in final states with a photon and a jet [13, 14].

The dynamics of the underlying photon+jet production processes in $2 \rightarrow 2$ hard collinear scattering can be investigated using the variable θ^*, where $\cos\theta^* \equiv \tanh(\Delta y/2)$ and Δy is the difference between the rapidities of the two final-state particles. The variable θ^* coincides with the scattering polar angle in the centre-of-mass frame for collinear scattering of massless particles, and its distribution is sensitive to the

spin of the exchanged particle. The distribution of the invariant mass of the leading photon and the leading jet ($m^{\gamma-\text{jet}}$) is also used to study the event dynamics since it is predicted in QCD to be monotonically decreasing for increasing values of $m^{\gamma-\text{jet}}$ in the absence of resonances that decay into a photon and a jet.

Prospects are presented for prompt photon and jet production in pp collisions at $\sqrt{s}$ = 14 TeV and $\sqrt{s}$ = 27 TeV in terms of cross sections for inclusive isolated photons and for photon+jet events as well as inclusive jet and dijet production cross sections. For inclusive isolated photons, expectations for the cross section differentially in E_{T}^{γ} in different ranges in photon pseudorapidity (η^{γ})[1] are presented. For photon+jet events, estimations for the cross section differentially in E_{T}^{γ}, $p_{\text{T}}^{\text{jet}}$, $\cos\theta^{*}$ and $m^{\gamma-\text{jet}}$ are presented. The jet production study is presented in terms of double differential cross sections for inclusive jet transverse momentum and the dijet system mass binned in jet rapidity and half absolute rapidity difference between the two leading jets, respectively. The upper-end reach of the energetic observables, such as E_{T}^{γ}, $p_{\text{T}}^{\text{jet}}$, $m^{\gamma-\text{jet}}$ and m_{jj}, is determined and the extension with respect to the latest measurements by the ATLAS Collaboration is emphasized [15–17].

In addition, this note presents a study of the uncertainties in the inclusive jet cross sections related to the uncertainties in the measurement of the jet energies in proton-proton collisions at $\sqrt{s}$ = 14 TeV for jets with $p_{\text{T}} > 100$ GeV and within $|y| < 3$.

2 The ATLAS detector and the High-Luminosity and High-Energy LHC

The ATLAS experiment [18] at the LHC is a multi-purpose particle detector with a forward-backward symmetric cylindrical geometry and a near 4π coverage in solid angle. It consists of an inner tracking detector surrounded by a thin superconducting solenoid providing a 2 T axial magnetic field, electromagnetic and hadron calorimeters, and a muon spectrometer. The inner tracking detector covers the pseudorapidity range $|\eta| < 2.5$. It consists of silicon pixel, silicon micro-strip, and transition radiation tracking detectors. Lead/liquid-argon (LAr) sampling calorimeters provide electromagnetic (EM) energy measurements with high granularity. A hadron (steel/scintillator-tile) calorimeter covers the central pseudorapidity range ($|\eta| < 1.7$). The end-cap and forward regions are instrumented with LAr calorimeters for both EM and hadronic energy measurements up to $|\eta| = 4.9$. The muon spectrometer surrounds the calorimeters and is based on three large air-core toroidal superconducting magnets with eight coils each. The field integral of the toroids ranges between 2.0 and 6.0 T m across most of the detector. The muon spectrometer includes a system of precision tracking chambers and fast detectors for triggering. A two-level trigger system, custom hardware followed by a software-based level, is used for online event selection and to reduce the event rate to about 1 kHz for offline reconstruction and storage.

The HL-LHC will operate at an instantaneous luminosity up to 7.5×10^{34} cm^{-2}s^{-1} that corresponds to an average number of inelastic proton-proton collisions per bunch-crossing $\langle\mu\rangle$ of 200. The HL-LHC conditions will demand a performance from the ATLAS detector that is well beyond the original design. An upgrade of all major ATLAS sub-detectors is needed before the start of this new phase to cope with the high-radiation environment and the large increase in pileup. The new Inner Tracker (ITk) [19, 20] will

[1] ATLAS uses a right-handed coordinate system with its origin at the nominal interaction point (IP) in the centre of the detector and the z-axis along the beam pipe. The x-axis points from the IP to the centre of the LHC ring, and the y-axis points upwards. Cylindrical coordinates (r, ϕ) are used in the transverse plane, ϕ being the azimuthal angle around the z-axis. The pseudorapidity is defined in terms of the polar angle θ as $\eta = -\ln\tan(\theta/2)$. Angular distance is measured in units of $\Delta R \equiv \sqrt{(\Delta\eta)^2 + (\Delta\phi)^2}$.

extend the ATLAS tracking capabilities to pseudorapidity $|\eta| < 4.0$. The upgraded Muon Spectrometer [21] with a forward muon tagger included will also provide lepton identification capabilities to $|\eta| < 4.0$. The new high granularity timing detector (HGTD) [22] designed to mitigate the pileup effects is foreseen in the forward region of $2.4 < |\eta| < 4.0$. The electronics of both LAr [23] and Tile [24] calorimeters will be upgraded to cope with longer latencies needed by the trigger system at such harsh pileup conditions. An upgraded TDAQ system [25] based on a hardware trigger with a maximum rate of 1 MHz and 10 ms latency and software-based reconstruction will send event data into storage at up to 10 kHz rate. A study of the expected performance of the upgraded ATLAS detector at the HL-LHC is reported in Ref. [26].

The HE-LHC target luminosity is 2.5×10^{35} cm^{-1}s^{-1}. The HE-LHC will employ the dipole magnets with a field of 16 T developed in the framework of the Future Circular Collider project [27]. The HE-LHC could accommodate two high-luminosity interaction-points at the locations of the ATLAS and CMS experiments [28]. It will allow to study new physics scenarios beyond the reach of the 14 TeV collider.

3 Analysis

3.1 Photon Analysis

The study of photon production is done via the analysis of inclusive isolated photons and that of photon production in association with at least one jet. In both analyses the photon is required to have a transverse energy in excess of 400 GeV and the pseudorapidity to lie in the range $|\eta^\gamma| < 2.37$ excluding the region $1.37 < |\eta^\gamma| < 1.56$. The photon is required to be isolated by imposing an upper limit on the amount of transverse energy inside a cone of size $\Delta R = 0.4$ in the η–ϕ plane around the photon, excluding the photon itself: $E_{\mathrm{T}}^{\mathrm{iso}} < E_{\mathrm{T,max}}^{\mathrm{iso}}$.

In the inclusive photon analysis, the goal is the measurement of the differential cross section as a function of E_{T}^{γ} in four regions of the photon pseudorapidity: $|\eta^\gamma| < 0.6$, $0.6 < |\eta^\gamma| < 1.37$, $1.56 < |\eta^\gamma| < 1.81$ and $1.81 < |\eta^\gamma| < 2.37$. Photon isolation is enforced by requiring $E_{\mathrm{T}}^{\mathrm{iso}} < 4.2 \cdot 10^{-3} \cdot E_{\mathrm{T}}^{\gamma} + 4.8$ GeV.

In the photon+jet analysis, jets are reconstructed using the anti-k_t algorithm [29] with a radius parameter $R = 0.4$. Jets overlapping with the photon are not considered if the jet axis lies within a cone of size $\Delta R = 0.8$ from the photon. The leading jet is required to have transverse momentum above 300 GeV and rapidity in the range $|y^{\mathrm{jet}}| < 2.37$. No additional condition is used for the differential cross sections as functions of E_{T}^{γ} and $p_{\mathrm{T}}^{\mathrm{jet}}$. For the differential cross sections as functions of the invariant mass of the photon+jet system and $|\cos\theta^*|$, additional constraints are imposed: $m^{\gamma-\mathrm{jet}} > 1.45$ TeV, $|\cos\theta^*| < 0.83$ and $|\eta^\gamma \pm y^{\mathrm{jet}}| < 2.37$. These additional constraints are imposed to remove the bias due to the rapidity and transverse-momentum requirements on the photon and the leading jet [30, 31]. Photon isolation is enforced by requiring $E_{\mathrm{T}}^{\mathrm{iso}} < 4.2 \cdot 10^{-3} \cdot E_{\mathrm{T}}^{\gamma} + 10$ GeV.

The yields of inclusive isolated photons and of photon+jet events are estimated using the program Jetphox 1.3.1_2 [32, 33]. This program includes a full next-to-leading-order QCD calculation of both the direct-photon and fragmentation contributions to the cross sections for the $pp \to \gamma$+X and $pp \to \gamma$+jet+X reactions. The number of massless quark flavours is set to five. The renormalisation (μ_{R}), factorisation (μ_{F}) and fragmentation (μ_{f}) scales are chosen to be $\mu_{\mathrm{R}} = \mu_{\mathrm{F}} = \mu_{\mathrm{f}} = E_{\mathrm{T}}^{\gamma}$. The calculations are performed using the MMHT2014 [34] parameterisations of the proton parton distribution functions (PDFs) and the BFG set II of parton-to-photon fragmentation functions at NLO [35]. Predictions are also obtained with

other PDF sets, namely CT14 [36], HERAPDF2.0 [37], NNPDF3.0 [38] and PDF4LHC HL-LHC [39]. The strong coupling constant $\alpha_s(m_Z)$ is set to the value assumed in the fit to determine the PDFs.

The reliability of the estimated yields using the program JETPHOX is supported by the high purity of the signal photons and the fact that the NLO QCD predictions describe adequately the measurements of these processes using pp collisions at $\sqrt{s}$ = 13 TeV [15, 16].

3.2 Jet Analysis

3.2.1 Experimental analysis

Jets are reconstructed using the anti-k_t algorithm with distance parameter R = 0.4 as implemented in the FastJet software package [40]. Jets are calibrated following the procedure described in [41]. The four momenta of the jets are recalculated to originate from the hard-scatter vertex rather than from the centre of the detector. The jet energy is corrected for the effect of pile-up using jet area-based correction together with residual number of primary vertices (N_{PV})- and $\langle\mu\rangle$-dependent correction as described in [42]. In addition, a jet energy- and η-dependent correction is applied. It is derived from Monte Carlo (MC) simulation and is designed to lead to agreement in energy and direction between reconstructed jets and particle jets on average. Further jet calibration steps applied in Run-2 measurements, namely the Global Sequential Calibration (GSC) [43] and the in situ calibration [41] are not derived and used in the current study. The GSC reduces effects from fluctuations in the composition of particles forming a jet and fluctuations in the hadronic shower caused by interactions of the hadrons with dead material in the calorimeter. An in situ correction is applied on data to remove residual differences in energy response between data and MC simulation evaluated using techniques where the p_T of the jet is balanced against well-measured objects, for example in photon+jet and Z-boson+jet events.

The total jet energy scale (JES) uncertainty in Run-2 measurements is compiled from 88 sources that all need to be propagated through the analysis in order to correctly account for uncertainty correlations in the jet calibration.

A reduced set of uncertainty components (nuisance parameters) is derived from eigenvectors and eigenvalues of the diagonalised total JES covariance matrix on the jet-level. The globally reduced configuration with 19 nuisance parameters (NPs) is used in this study. Eight NPs coming from the in situ techniques are related to the detector description, physics modelling and measurements of the Z/γ energies in ATLAS calorimeters. Three describe the physics modelling and the statistics of the dijet MC sample and the non-closure of the method, used to derive the η-intercalibration [41]. The single-hadron response studies [44] are used to describe the JES uncertainty in the high-p_T jet regions, where the in situ studies have limited statistics. Four NPs are due to the pile-up corrections of the jet kinematics, that take into account mis-modelling of N_{PV} and $\langle\mu\rangle$ distributions, dependence of the average energy density, ρ, on the pileup activity in a given event, ρ-topology, and the residual p_T dependence. Finally, two uncertainty components take into account the difference in the calorimeter response to the quark- and gluon-initiated jets (flavour response) and the jet flavour composition, and one uncertainty in the correction for the energy leakage beyond the calorimeter, the "punch-through" effect.

In order to estimate the precision in the jet cross section measurements at the HL-LHC three scenarios of possible uncertainties in the jet energy scale calibration are defined.

In all three scenarios, the high-p_{T} uncertainty, the punch-through uncertainty and the flavour composition uncertainty are considered to be negligible. The JES uncertainty in the high-p_{T} range will be accessed using the multi-jet balance (MJB) method, rather than single hadron response measurements, since the high statistics at the HL-LHC will allow precision JES measurements in the high-p_{T} region. Flavour composition and flavour response uncertainties are driven by the MC generator differences. With advances in the MC models and tuning of their parameters these uncertainties could be significantly reduced. The flavour composition uncertainty is therefore ignored to study the maximal impact of the expected improvements on the modelling of parton showers and hadronisation on precision jet energy measurements. The flavour response uncertainties are kept at the same value as in Run-2 or reduced by a factor of two in conservative and optimistic scenarios, respectively.

The pile-up uncertainties, except the ρ-topology uncertainty, are considered to be negligible. Current small uncertainties in the JES due to mis-modelling of N_{PV} and $\langle\mu\rangle$ distributions and the residual p_{T} dependence lead to very small uncertainties at the HL-LHC conditions. With the advances of new pile-up rejection techniques the ρ-topology uncertainty could be maintained at a level comparable to the one in Run-2 or reduced by a factor of two. This is addressed in conservative and optimistic scenarios.

Since the Run-2 jet energy resolution (JER) uncertainty estimation is conservative, the final Run-2 JER uncertainty is expected (based on Run-1 experience) to be about twice as small as the current one. Therefore, the JER uncertainty is estimated to be half of that in Run-2.

The rest of uncertainty sources are fixed in different scenarios as follows:

- Conservative scenario:
  - All in situ components are kept at the same value as in Run-2, except the uncertainties related to the photon energy measurement in the high-E_{T} range and the MJB method uncertainties. These uncertainties are reduced by a factor of two, since they are expected to be improved at the HL-LHC.
  - MC modelling uncertainty in the η-intercalibration is reduced by a factor of two while the other two are neglected. Currently, MC modelling uncertainty is derived by comparison of leading-order (LO) pQCD generators. In future, with advances in MC generators development, this uncertainty is expected to be reduced.
  - Flavour response uncertainty is set to the Run-2 value;
  - ρ-topology uncertainty is unchanged compared to Run-2 results;
- Optimistic scenario:
  - All in situ components are treated identically to the conservative scenario;
  - All three uncertainty sources in the η-intercalibration method are ignored;
  - Flavour response uncertainty is reduced by a factor of two compared to Run-2 results;
  - ρ-topology uncertainty is two times smaller as in Run-2;
- Pessimistic scenario:
  - same as optimistic scenario, but all uncertainty sources of in situ methods are retained from Run-2.

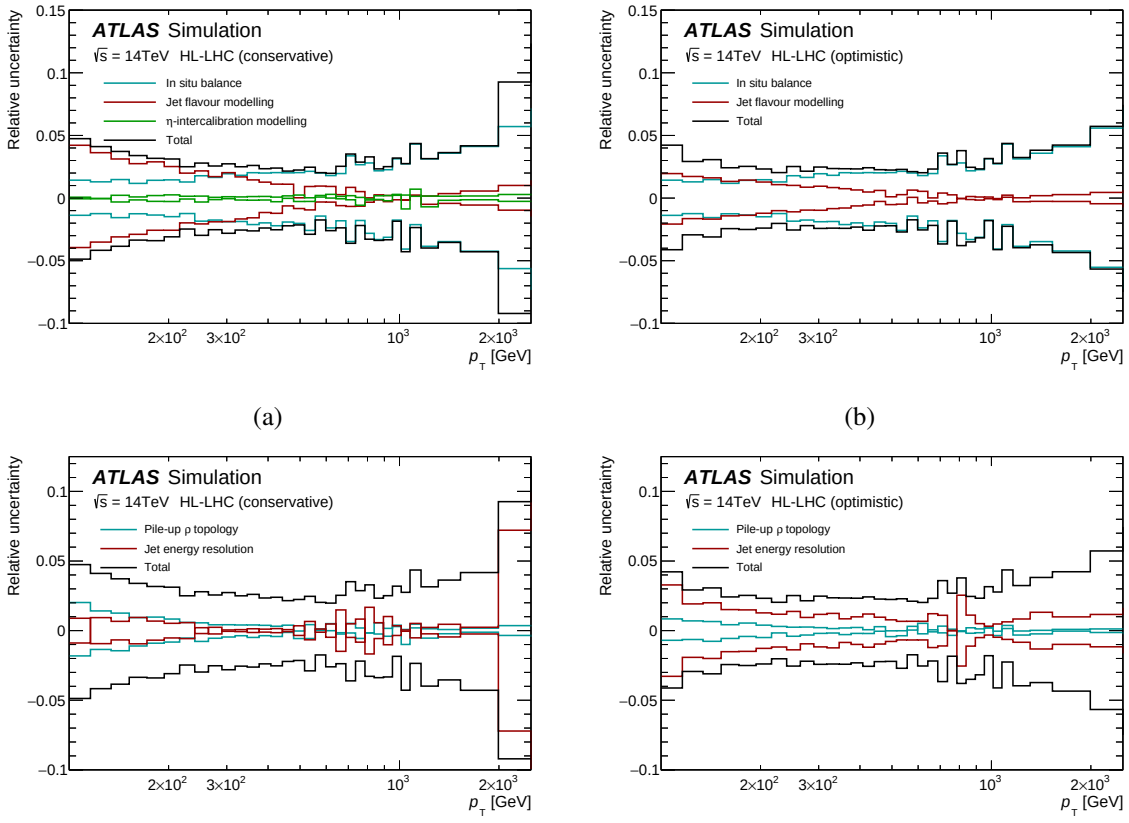

Figure 1: Relative systematic uncertainty for (a,c) conservative and (b,d) optimistic scenarios in the inclusive jet cross sections as a function of jet p_{T} in the $|y| < 3$ rapidity region. The individual uncertainty components are shown in different colours. The total systematic uncertainty, calculated by adding the individual uncertainties in quadrature, is shown as a black line.

All components of the JES uncertainty are propagated from the jet-level to the cross section level as follows. The jet p_{T} is scaled up and down by one standard deviation of each source of uncertainty. The difference between the nominal reco-level spectrum and the systematically shifted one is taken as a systematic uncertainty. All JES uncertainties are treated as bin-to-bin correlated and independent from each other in this procedure. The unfolding of the detector-level distributions to the particle-level spectrum is not performed is this study. A possible modification of the shapes of uncertainty components during the unfolding procedure is expected to be small and neglected in this study.

The inclusive jet cross sections in this section are studied as a function of the jet transverse momentum for jets with $p_{\mathrm{T}} > 100$ GeV and within $|y| < 3$.

The estimation of the JES uncertainty in the measurements of inclusive jet cross section at the HL-LHC for three JES uncertainty scenarios are presented in Figure 1.

3.2.2 Fixed-order predictions and PDF sensitivity

Theoretical predictions at NLO QCD are calculated using MCFM [45] interfaced to APPLgrid [46] for fast convolution with PDFs. The renormalisation and factorisation scales are set to $\mu_{\mathrm{R}} = \mu_{\mathrm{F}} = p_{\mathrm{T}}^{\mathrm{jet}}$ for the inclusive jet cross section and $\mu_{\mathrm{R}} = \mu_{\mathrm{F}} = m_{\mathrm{jj}}$ for the dijet mass distribution. The predictions are calculated using CT14nnlo [36] PDF set provided by the LHAPDF6 [47].

The main uncertainties in the NLO predictions come from uncertainties associated with the PDFs, the choice of renormalisation and factorisation scales, and the uncertainty in the value of the strong coupling. PDF uncertainties are defined at the 68% CL and propagated through the calculations following the prescription given by the PDF set authors. The nominal scales are independently varied up or down by a factor of two in both directions excluding opposite variations of μ_R and μ_F. The envelope of resulting variations of the predicted cross section is taken as the total scale uncertainty. The uncertainty from α_s is evaluated by calculating the cross sections using two PDF sets that differ only on the value of the strong coupling at M_Z and then scaling the cross section difference corresponding to an uncertainty $\Delta\alpha_s = 0.0015$ [48].

The inclusive jet cross sections are studied double-differentially as a function of the jet transverse momentum and absolute jet rapidity while the dijet production cross sections are presented as a function of the invariant mass of the dijet system and as a function of half the absolute rapidity separation between the two highest-p_{T} jets satisfying $|y| < 3$, denoted y^*. In both analyses the leading jet is required to be within $|y| < 3$ and to have $p_{\mathrm{T}} > 100$ GeV. The other jets are required to be in the same rapidity range with $p_{\mathrm{T}} > 75$ GeV.

Figures 2 and 3 shows the theoretical uncertainties, calculated using CT14 [36] PDF set, in the inclusive jet and dijet cross sections for representative phase-space regions at $\sqrt{s} = 14$ and 27 TeV, respectively. The total uncertainty is about 5 % in the low- and intermediate p_{T} and m_{jj} regions, growing to 20–40% in the high-p_{T} and dijet mass ranges.

Measurements of weak boson [49], top quark [50], photon, jet productions [51] (and many others) at the LHC have been already used as inputs to global PDF fits [34, 36, 52, 53] in determination of the proton structure. High precision LHC data have allowed to further constrain the knowledge of the proton content by extending the coverage of PDF-related phase space in measurements and to significantly reduce PDF uncertainties.

A study to estimate the impact of future PDF-sensitive measurements at the HL-LHC on the precision of PDFs determination was performed in Ref. [39]. Three possible scenarios for the experimental systematic uncertainties were considered. This study concluded that HL-LHC measurements will further reduce the PDF uncertainties and published the dedicated PDF sets, PDF4LHC HL-LHC, where the HL-LHC pseudo-data were included in the fits.

Figure 4 and 5 present the comparison of inclusive jet and dijet production cross sections calculated using different PDF sets at $\sqrt{s} = 14$ and 27 TeV, respectively. It shows 5–10% difference between central values in the low- and intermediate-p_{T} and m_{jj} regions, however these predictions are still compatible with the quoted PDF uncertainty. The differences between various PDF sets predictions in the high-p_{T} and m_{jj} range highlights the expected constraining power of future measurements at the HL-LHC and HE-LHC.

Figure 6 and 7 depict the comparison of PDF uncertainties in the inclusive jet and dijet production cross sections for CT14 and PDF4LHC HL-LHC (optimistic scenario) in the pp collisions at $\sqrt{s} = 14$ and

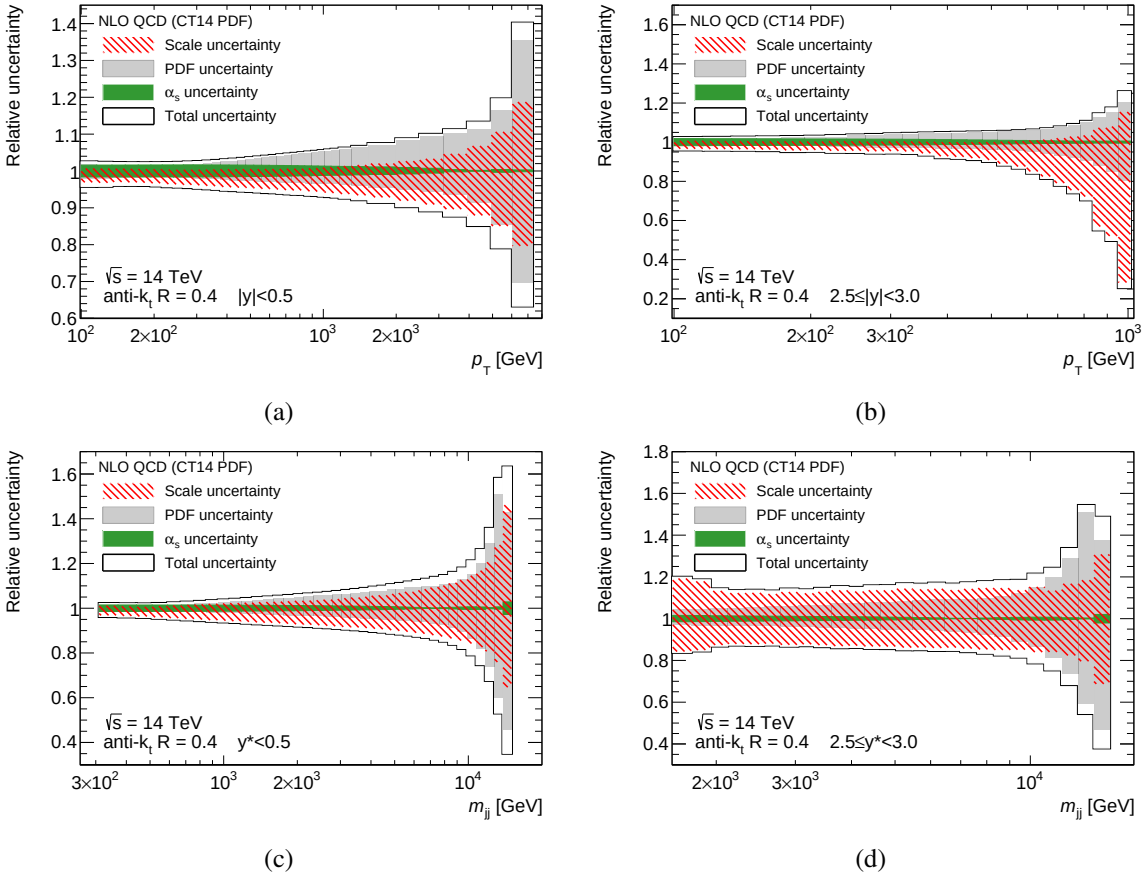

Figure 2: Relative NLO QCD uncertainties in the (a,b) inclusive jet and (c,d) dijet cross sections calculated using the CT14 PDF set at $\sqrt{s} = 14$ TeV. Panels (a,c) and (b,d) correspond to the first and last $|y|$ and y^* bins in measurements, respectively. The uncertainties due to the renormalisation and factorisation scale, α_s, PDF and the total uncertainty are shown. The total uncertainty, calculated by adding the individual uncertainties in quadrature, is shown as a black line.

27 TeV. A significant improvement in PDF extraction is expected with the inclusion of PDF-sensitive measurements at the HL-LHC in PDF fits.

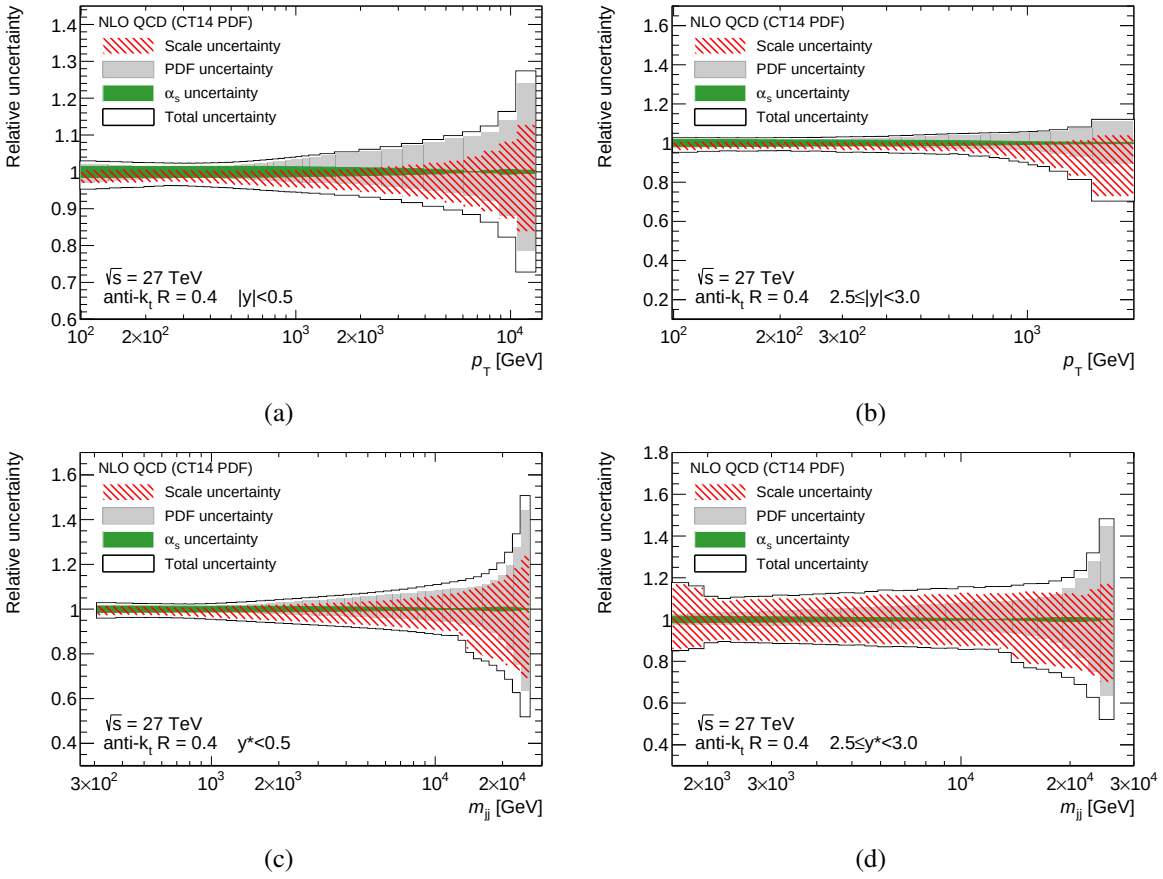

Figure 3: Relative NLO QCD uncertainties in the (a,b) inclusive jet and (c,d) dijet cross sections calculated using the CT14 PDF set at $\sqrt{s} = 27$ TeV. Panels (a,c) and (b,d) correspond to the first and last $|y|$ and y^* bins in measurements, respectively. The uncertainties due to the renormalisation and factorisation scale, α_s, PDF and the total uncertainty are shown. The total uncertainty, calculated by adding the individual uncertainties in quadrature, is shown as a black line.

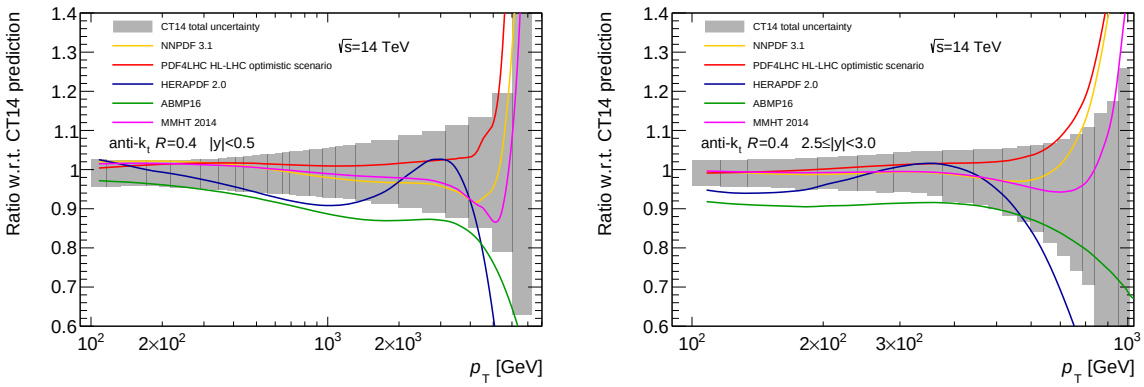

(a) $|y| < 0.5$

(b) $2.5 < |y| < 3.0$

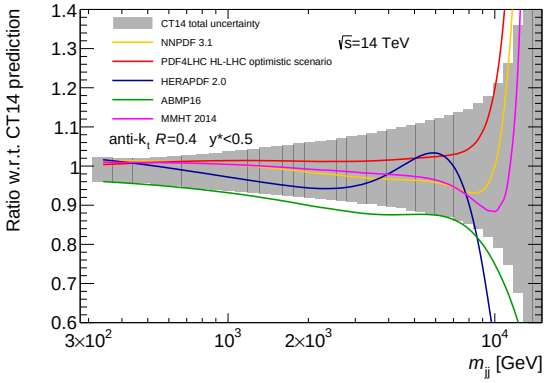

(c) $y^* < 0.5$

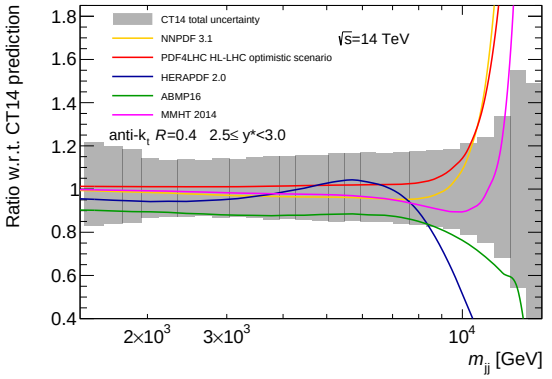

(d) $2.5 < y^* < 3.0$

Figure 4: Ratio of cross sections calculated using NNPDF 3.1 [52], MMHT 2014 [34], ABMP 16 [53], PDF4LHC HL-LHC [39], to one using CT14 [36] PDFs in the (a,b) inclusive jet and (c,d) dijet cross sections at $\sqrt{s}$ = 14 TeV. Panels (a,c) and (b,d) correspond to the first and last $|y|$ and y^* bins in measurements, respectively. The gray band depicts the total NLO pQCD uncertainty in cross section calculated using CT14 [36] PDF set.

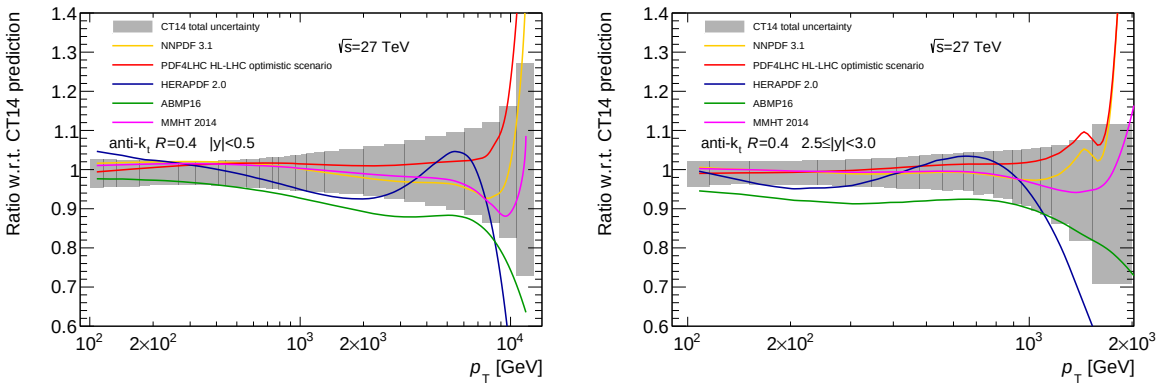

(a) $|y| < 0.5$

(b) $2.5 < |y| < 3.0$

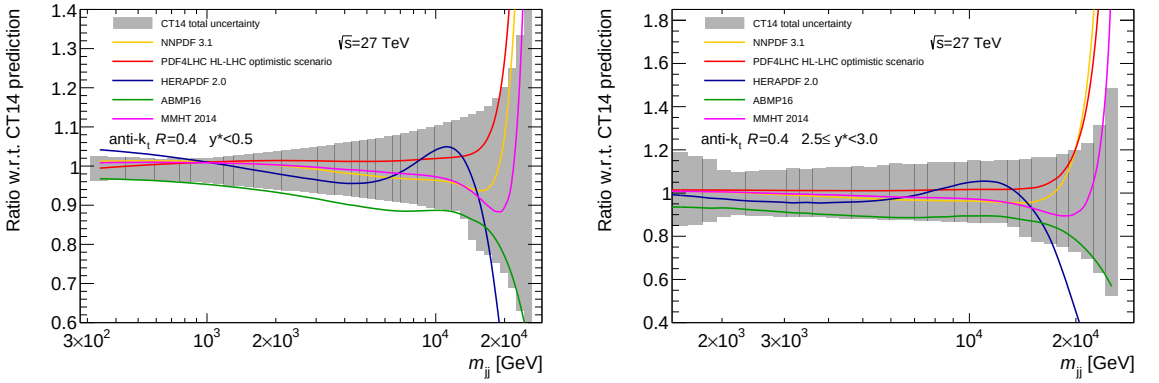

(c) $y^* < 0.5$

(d) $2.5 < y^* < 3.0$

Figure 5: Ratio of cross sections calculated using NNPDF 3.1 [52], MMHT 2014 [34], ABMP 16 [53], PDF4LHC HL-LHC [39], to one using CT14 [36] PDFs in the (a,b) inclusive jet and (c,d) dijet cross sections at $\sqrt{s}$ = 27 TeV. Panels (a,c) and (b,d) correspond to the first and last $|y|$ and y^* bins in measurements, respectively. The gray band depicts the total NLO pQCD uncertainty in cross section calculated using CT14 PDF set.

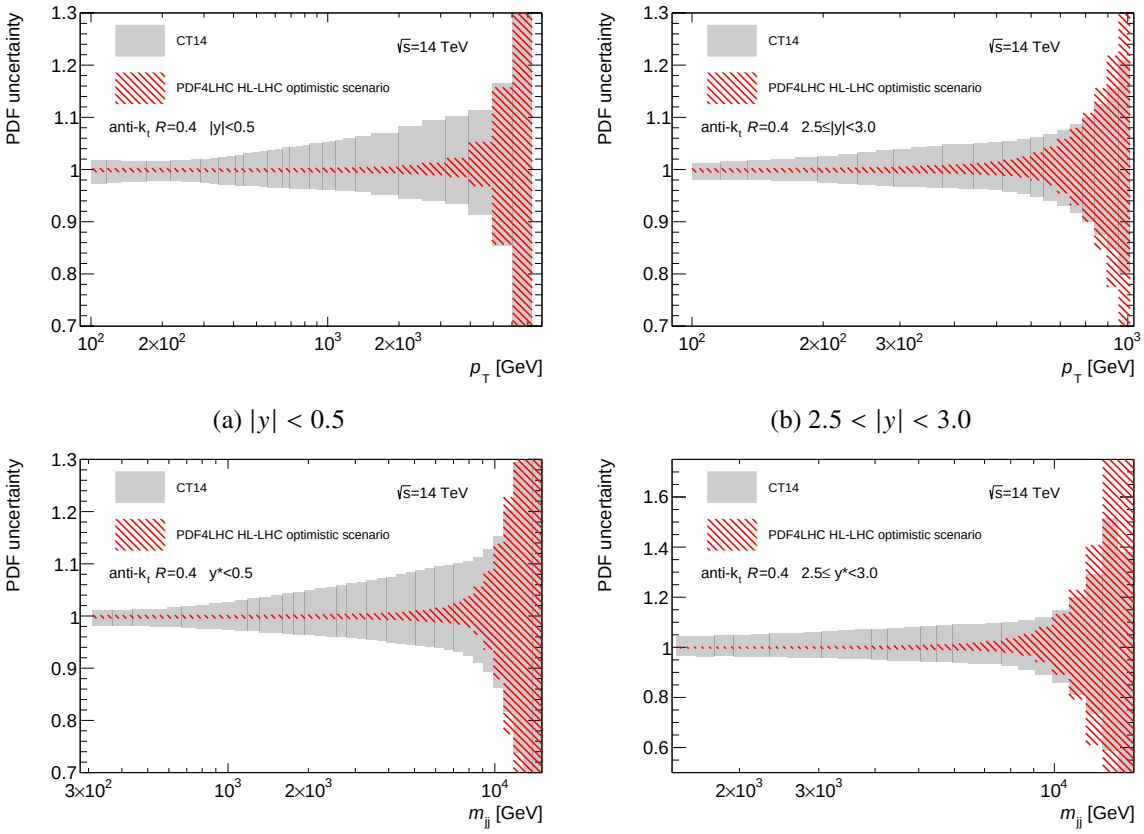

(a) $|y| < 0.5$ (b) $2.5 < |y| < 3.0$

(c) $y^* < 0.5$ (d) $2.5 < y^* < 3.0$

Figure 6: Comparison of the PDF uncertainty in the (a,b) inclusive jet and (c,d) dijet cross sections calculated using the CT14 PDF and PDF4LHC HL-LHC [39] sets at $\sqrt{s} = 14$ TeV. Panels (a,c) and (b,d) correspond to the first and last $|y|$ and y^* bins in measurements, respectively.

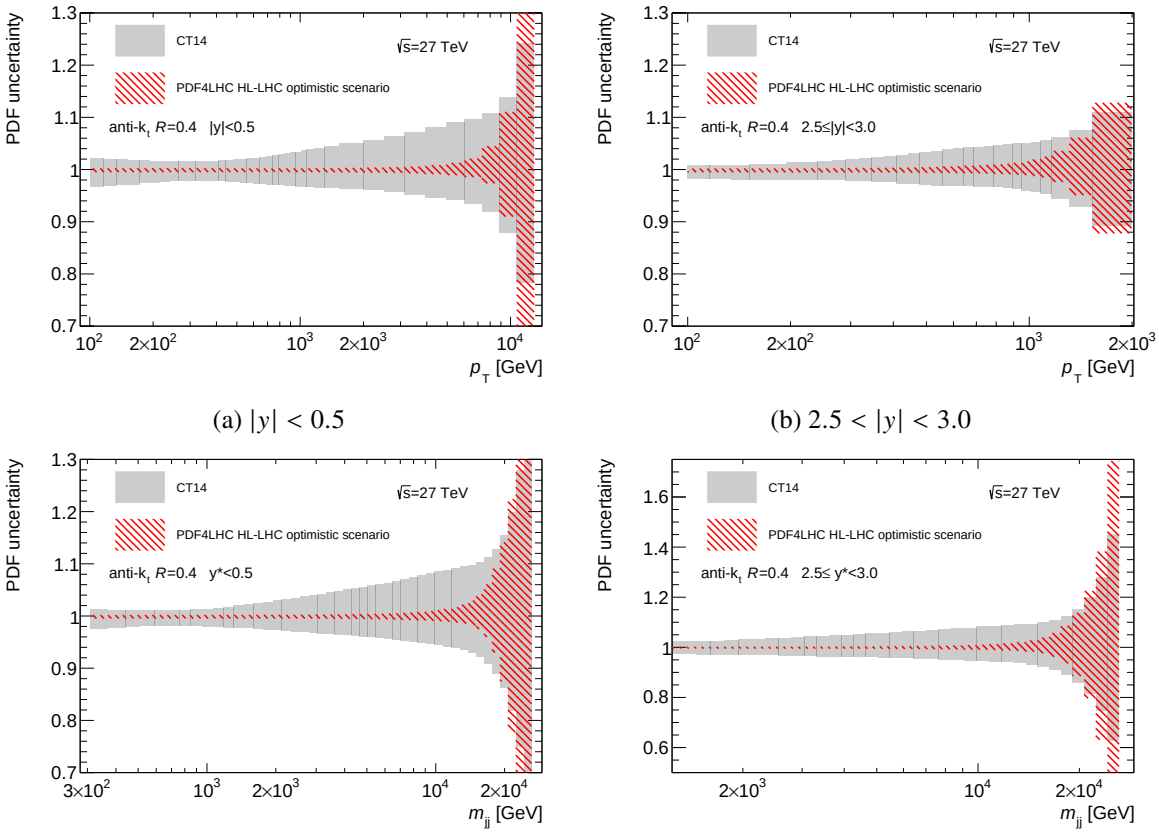

(a) $|y| < 0.5$ (b) $2.5 < |y| < 3.0$

(c) $y^* < 0.5$ (d) $2.5 < y^* < 3.0$

Figure 7: Comparison of the PDF uncertainty in the (a,b) inclusive jet and (c,d) dijet cross sections calculated using the CT14 PDF and PDF4LHC HL-LHC [39] sets at $\sqrt{s}$ = 27 TeV. Panels (a,c) and (b,d) correspond to the first and last $|y|$ and y^* bins in measurements, respectively.

3.2.3 Non-perturbative effects

The fixed-order predictions are obtained at the parton-level. The non-perturbative corrections (NPCs) are applied to bring the theoretical predictions from parton-level to particle-level in order to allow a comparison with the measured cross sections in data. The NPC are evaluated using Pythia v8.210 MC [54] generator with A14 [55] underlying event tune and the tune variations are used to evaluate the uncertainty in the NPC due to the differences in hadronisation and underlying event modelling.

Figures 8 to 11 show separate corrections for the hadronisation, underlying event as well as the total non-perturbative correction to the inclusive jet and dijet production cross section in pp collisions at $\sqrt{s}$ = 14 and 27 TeV.

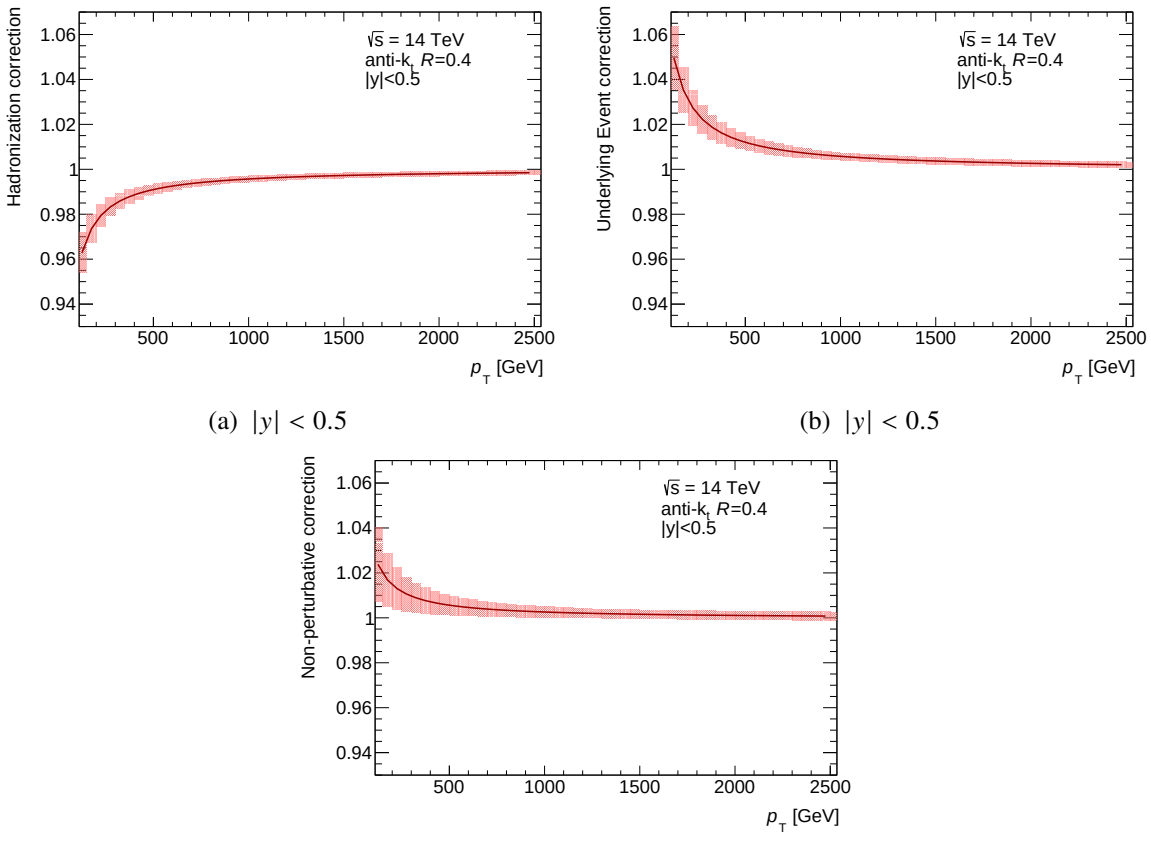

(a) $|y| < 0.5$ (b) $|y| < 0.5$

(c) $|y| < 0.5$

Figure 8: Non-perturbative corrections for the inclusive jet production cross section at $\sqrt{s}$ = 14 TeV in the $|y| < 0.5$ rapidity range. Separate (a) corrections for the hadronisation, (b) underlying event and (c) the total non-perturbative correction are shown.

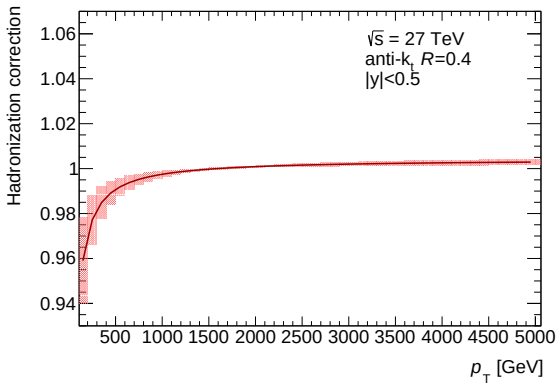

(a) $|y| < 0.5$

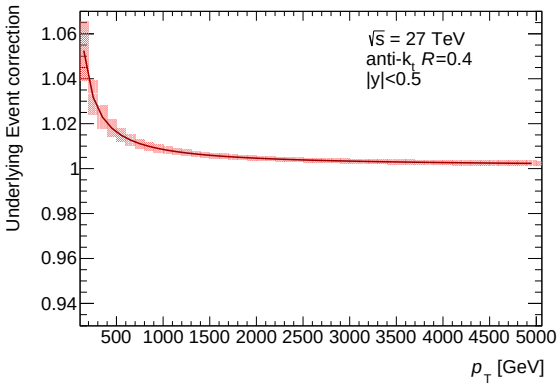

(b) $|y| < 0.5$

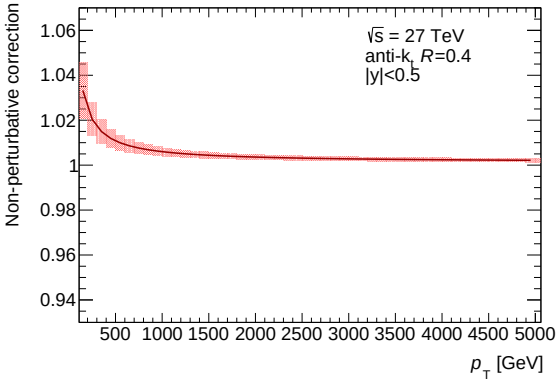

(c) $|y| < 0.5$

Figure 9: Non-perturbative corrections for the inclusive jet production cross section at $\sqrt{s} = 27$ TeV in the $|y| < 0.5$ rapidity range. Separate (a) corrections for the hadronisation, (b) underlying event and (c) the total non-perturbative correction are shown.

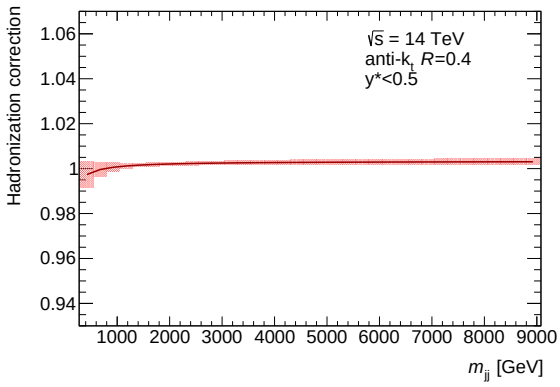

(a) $y^* < 0.5$

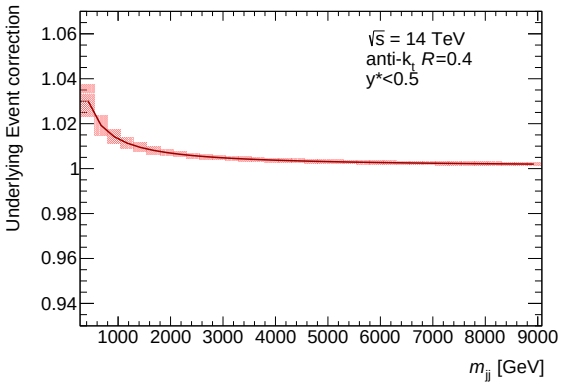

(b) $y^* < 0.5$

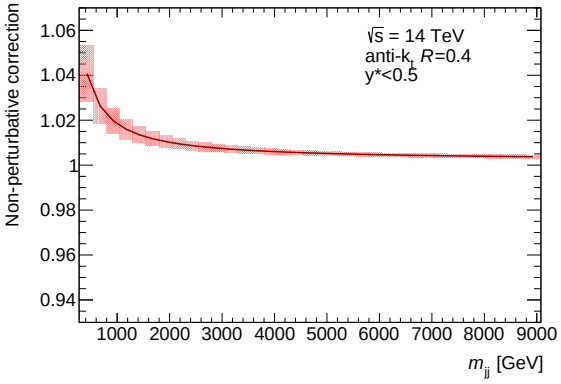

(c) $y^* < 0.5$

Figure 10: Non-perturbative corrections for the dijet production cross section at $\sqrt{s} = 14$ TeV in the $y^* < 0.5$ rapidity range. Separate (a) corrections for the hadronisation, (b) underlying event and (c) the total non-perturbative correction are shown.

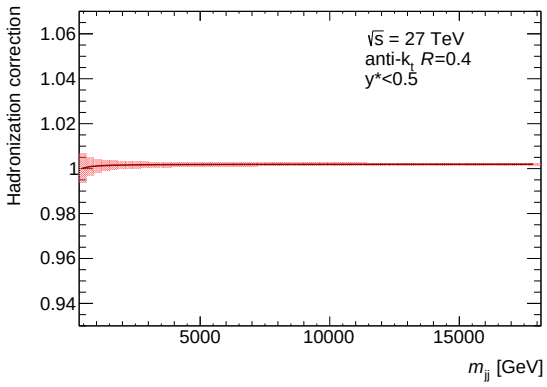

(a) $y^* < 0.5$

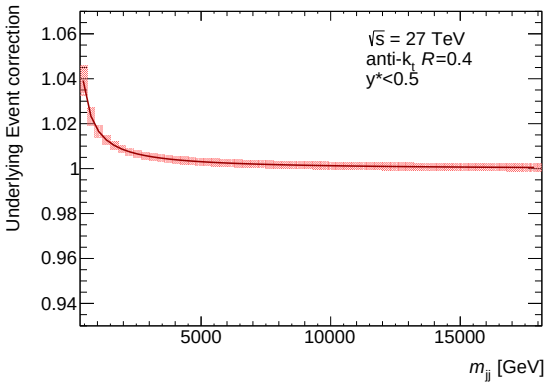

(b) $y^* < 0.5$

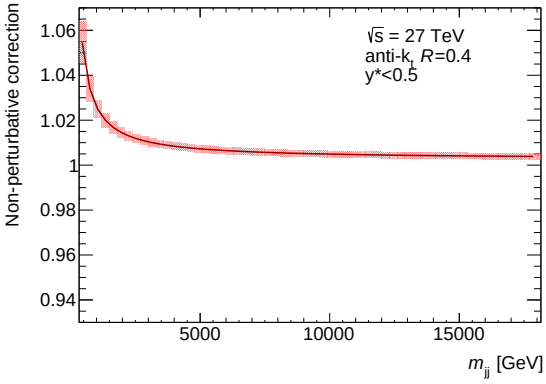

(c) $y^* < 0.5$

Figure 11: Non-perturbative corrections for the dijet production cross section at $\sqrt{s}$ = 27 TeV in the $y^* < 0.5$ rapidity range. Separate (a) correction for the hadronisation, (b) underlying event and (c) the total non-perturbative correction are shown.

The weak radiative corrections in the dijet production at $\sqrt{s}$ =14 TeV are calculated in Ref. [56]. This corrections can be of the order of several per-cents in the tails of kinematic distributions due to the Sudakov-type logarithms. The impact of these effects on the inclusive jet and dijet cross section predictions is not considered in this note.

4 Results

4.1 Photon Results

The predicted number of inclusive isolated photon events as a function of E_{T}^{γ} in the different ranges of $|\eta^{\gamma}|$ assuming an integrated luminosity of 3 ab^{-1} of pp collision data at $\sqrt{s}$ = 14 TeV is shown in Fig. 12. The predicted number of events above an E_{T}^{γ} threshold is shown in Fig. 13. The reach in E_{T}^{γ} is (a) 3–3.5 TeV for $|\eta^{\gamma}| < 0.6$, (b) 2.5–3 TeV for $0.6 < |\eta^{\gamma}| < 1.37$, (c) 1.5–2 TeV for $1.56 < |\eta^{\gamma}| < 1.81$ and (d) 1–1.5 TeV for $1.81 < |\eta^{\gamma}| < 2.37$. This represents a significant extension of the region measured so far with pp collisions at $\sqrt{s}$ = 13 TeV [15]; as an example, the E_{T}^{γ} reach is extended from 1.5 TeV to 3–3.5 TeV for $|\eta^{\gamma}| < 0.6$. The projected cross sections as a function of E_{T}^{γ} together with Run-2 results at $\sqrt{s}$ = 13 TeV [15] are shown in Fig. 14.

The sensitivity to the proton PDFs is studied in the ratio between the predicted cross sections with CT14, NNPDF3.0 and HERAPDF2.0 and those using MMHT2014. The ratios are shown in Fig. 15 and differences of up to 30% are seen. The predicted relative statistical uncertainty on the number of inclusive isolated photon events as a function of E_{T}^{γ} assuming an integrated luminosity of 3 ab^{-1} of collision data at $\sqrt{s}$ = 14 TeV in different ranges of photon pseudorapidity is shown in Fig. 16. A relative statistical uncertainty below 10% is achieved for photon transverse energies up to 2.5 TeV (1.5 TeV) for $|\eta^{\gamma}| < 0.6$ and $0.6 < |\eta^{\gamma}| < 1.37$ ($1.56 < |\eta^{\gamma}| < 1.81$ and $1.81 < |\eta^{\gamma}| < 2.37$).

The photon energy scale and resolution represent the dominant source of systematic uncertainty for the measurement of the inclusive isolated-photon cross section $d\sigma/dE_{\mathrm{T}}^{\gamma}$ in pp collisions at $\sqrt{s}$ = 13 TeV [15]. The size of this systematic uncertainty as estimated in Run-2 using 3.2 fb^{-1} of pp collision data is shown in Table 1 for selected regions. The aforementioned estimations of the systematic uncertainties due to the photon energy scale and resolution will possibly be improved by using Run-2 and Run-3 data. Furthermore, improvements in the systematic uncertainties are also expected from the HL-LHC data thanks to the increased statistics for the photon energy calibration and in situ determination of the photon identification and isolation efficiencies.

Table 1: Systematic uncertainty due to the photon energy scale (γ-ES) and resolution (γ-ER) for the measurement of the inclusive isolated-photon cross section $d\sigma/E_{\mathrm{T}}^{\gamma}$ in pp collisions at $\sqrt{s}$ = 13 TeV in different regions of $|\eta^{\gamma}|$ [15].

E_{T}^{γ} [GeV]	γ-ES and γ-ER systematic uncertainty (in %)			
	$\lvert\eta^{\gamma}\rvert < 0.6$	$0.6 < \lvert\eta^{\gamma}\rvert < 1.37$	$1.56 < \lvert\eta^{\gamma}\rvert < 1.81$	$1.81 < \lvert\eta^{\gamma}\rvert < 2.37$
400–470	+2.2, −2.2	+3.0, −2.9	+11, −9.3	+4.5, −4.4
750–900	+3.0, −2.8	+3.8, −3.8	+16, −15	+6.9, −6.5
900–1100	+3.3, −2.9	+4.1, −4.1	+18, −18	
1100–1500	+4.0, −3.1	+4.6, −4.6		

The predicted number of photon+jet events as a function of E_{T}^{γ}, $p_{\mathrm{T}}^{\mathrm{jet}}$, $m^{\gamma-\mathrm{jet}}$ and $|\cos\theta^{*}|$, assuming an integrated luminosity of 3 ab^{-1} of pp collision data at $\sqrt{s}$ = 14 TeV, is shown in Fig. 17. The predictions show that the reach in E_{T}^{γ} and $p_{\mathrm{T}}^{\mathrm{jet}}$ is 3.5 TeV and that the reach in $m^{\gamma-\mathrm{jet}}$ is 7 TeV. The predicted relative statistical uncertainty on the number of photon+jet events as a function of the different observables, assuming an integrated luminosity of 3 ab^{-1} of pp collision data at $\sqrt{s}$ = 14 TeV, is shown in Fig. 18. The relative statistical uncertainty is below 10% for (a) E_{T}^{γ} up to 2.5 TeV, (b) $p_{\mathrm{T}}^{\mathrm{jet}}$ up to 3 TeV and (c) $m^{\gamma-\mathrm{jet}}$ up to 6 TeV; for $|\cos\theta^{*}|$ the relative statistical uncertainty is below 1% for the entire range considered. In comparison to the latest ATLAS measurements at $\sqrt{s}$ = 13 TeV with 3.2 fb^{-1} of integrated luminosity [16], the projections presented here extend significantly the reach in several observables: for E_{T}^{γ} and $p_{\mathrm{T}}^{\mathrm{jet}}$ from 1.5 TeV to 3.5 TeV and for $m^{\gamma-\mathrm{jet}}$ from 3.3 TeV to 7 TeV.

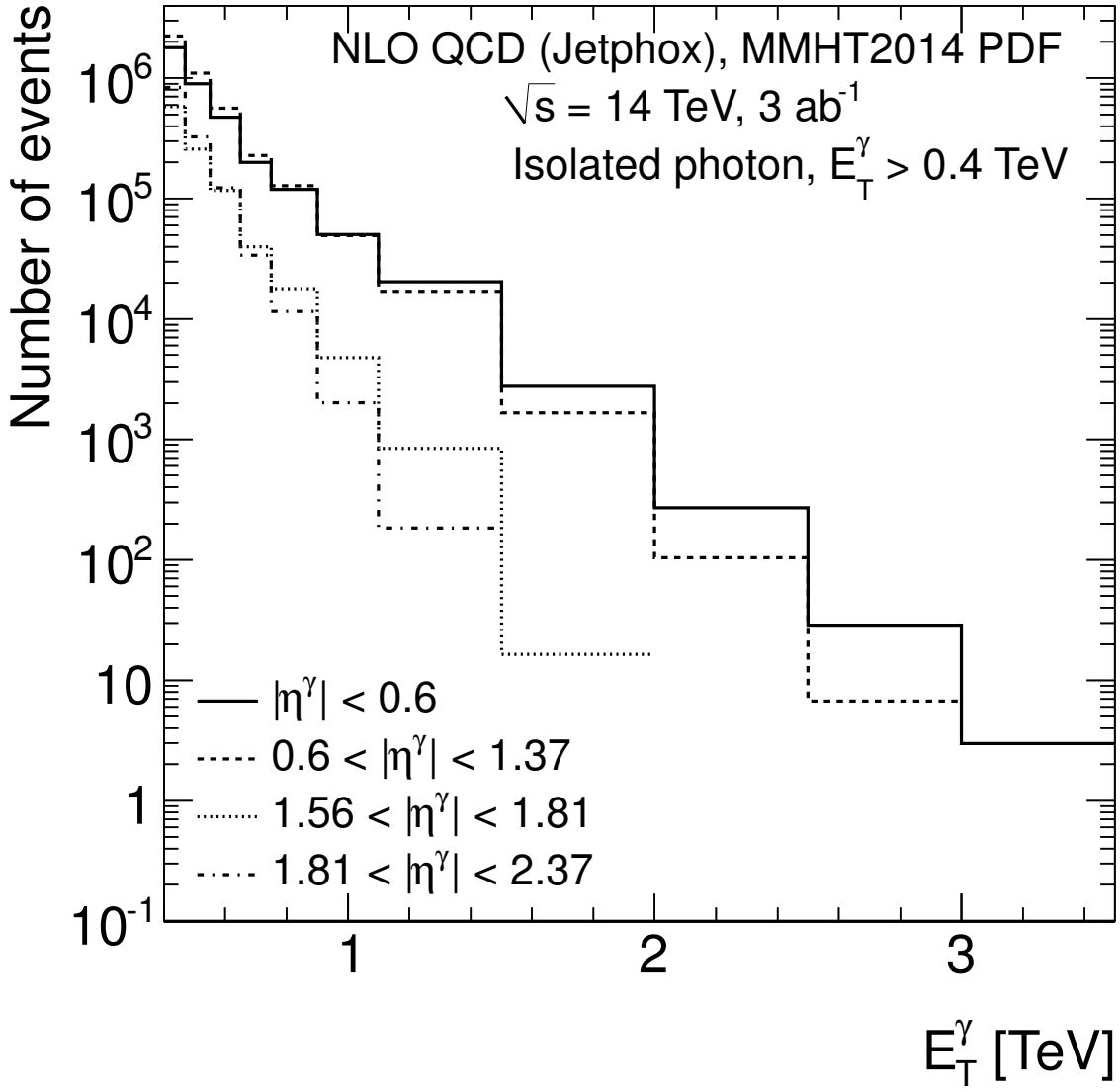

Figure 12: Predicted number of inclusive isolated photon events as a function of E_{T}^{γ} assuming an integrated luminosity of 3 ab^{-1} of pp collision data at $\sqrt{s}$ = 14 TeV in different ranges of photon pseudorapidity: $|\eta^{\gamma}| < 0.6$ (solid histogram), $0.6 < |\eta^{\gamma}| < 1.37$ (dashed histogram), $1.56 < |\eta^{\gamma}| < 1.81$ (dotted histogram) and $1.81 < |\eta^{\gamma}| < 2.37$ (dot-dashed histogram).

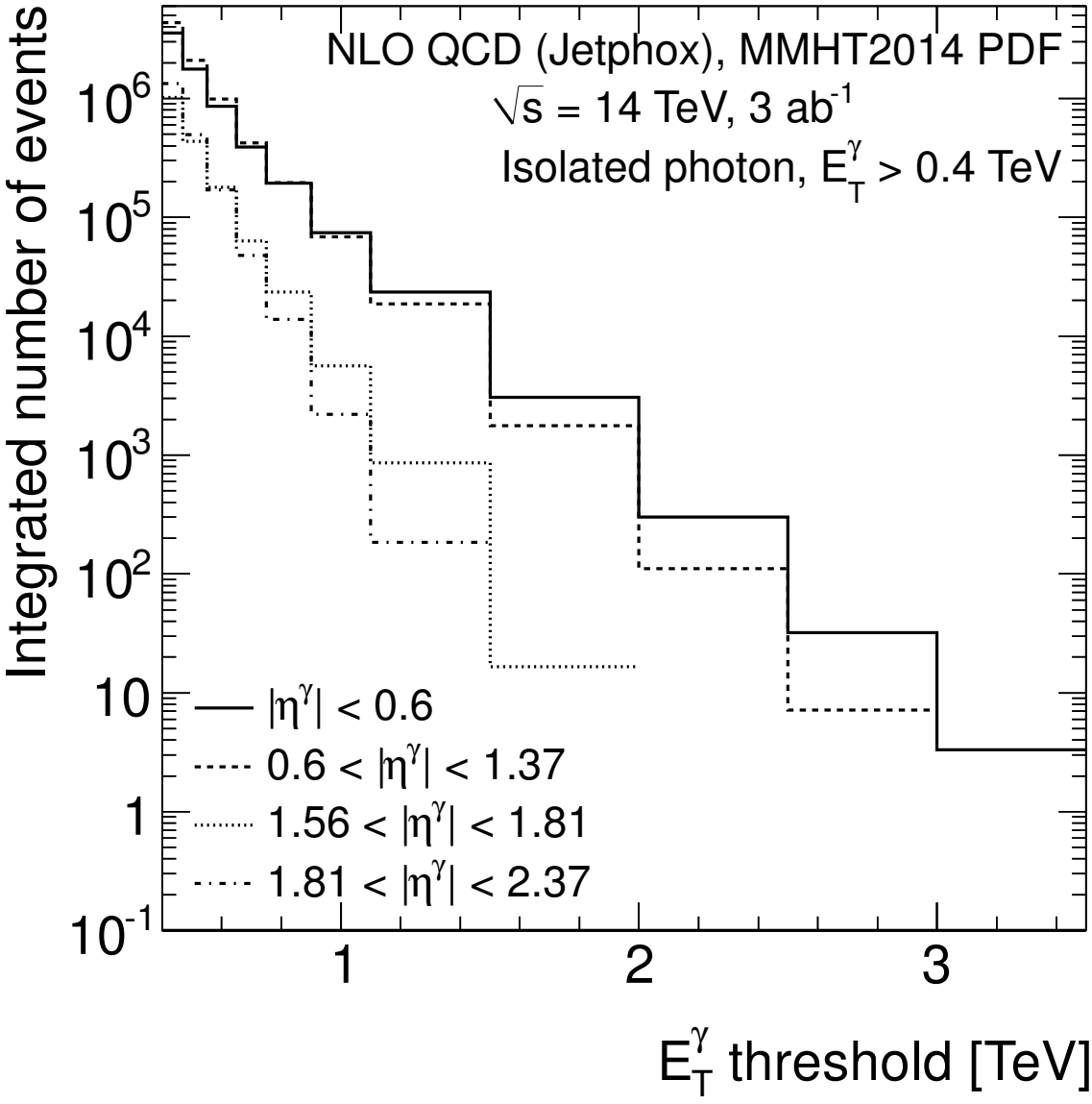

Figure 13: Predicted number of inclusive isolated photon events above an E_{T}^{γ} threshold assuming an integrated luminosity of 3 ab^{-1} of pp collision data at $\sqrt{s}$ = 14 TeV in different ranges of photon pseudorapidity: $|\eta^{\gamma}| < 0.6$ (solid histogram), $0.6 < |\eta^{\gamma}| < 1.37$ (dashed histogram), $1.56 < |\eta^{\gamma}| < 1.81$ (dotted histogram) and $1.81 < |\eta^{\gamma}| < 2.37$ (dot-dashed histogram).

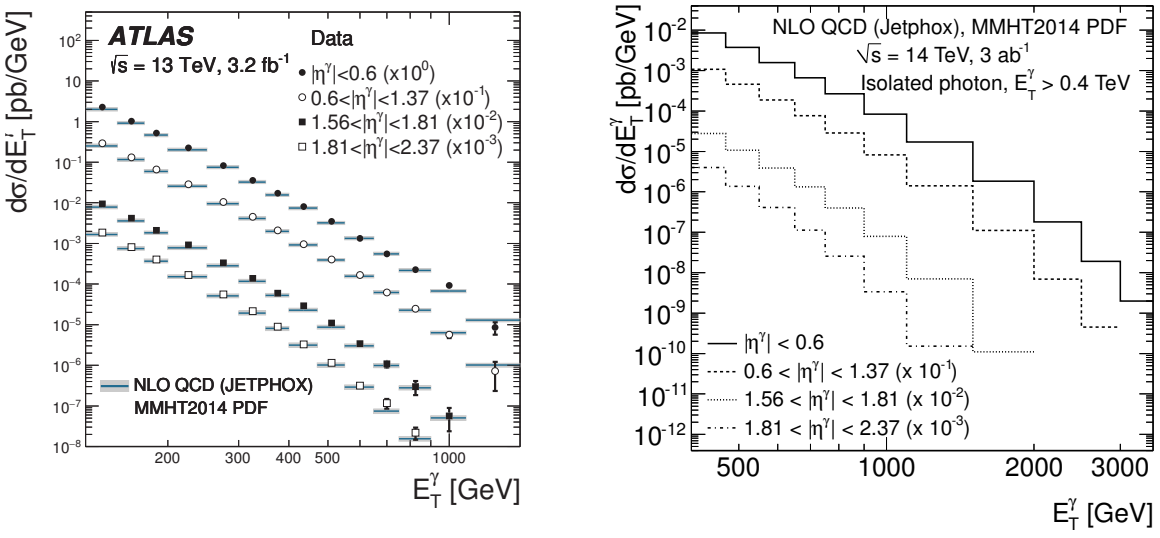

(a) (b)

Figure 14: (a) Measured cross sections in pp collisions at $\sqrt{s}$ = 13 TeV for isolated-photon production as functions of E_{T}^{γ} in $|\eta^{\gamma}| < 0.6$ (black dots), $0.6 < |\eta^{\gamma}| < 1.37$ (open circles), $1.56 < |\eta^{\gamma}| < 1.81$ (black squares) and $1.81 < |\eta^{\gamma}| < 2.37$ (open squares). The NLO QCD predictions from JETPHOX based on the MMHT2014 PDFs (solid lines) are also shown. The measurements and the predictions are normalised by the factors shown in parentheses to aid visibility. The error bars represent the statistical and systematic uncertainties added in quadrature. The shaded bands display the theoretical uncertainty. (b) Predicted cross section in pp collisions at $\sqrt{s}$ = 14 TeV in $|\eta^{\gamma}| < 0.6$ (solid histogram), $0.6 < |\eta^{\gamma}| < 1.37$ (dashed histogram), $1.56 < |\eta^{\gamma}| < 1.81$ (dotted histogram) and $1.81 < |\eta^{\gamma}| < 2.37$ (dot-dashed histogram).

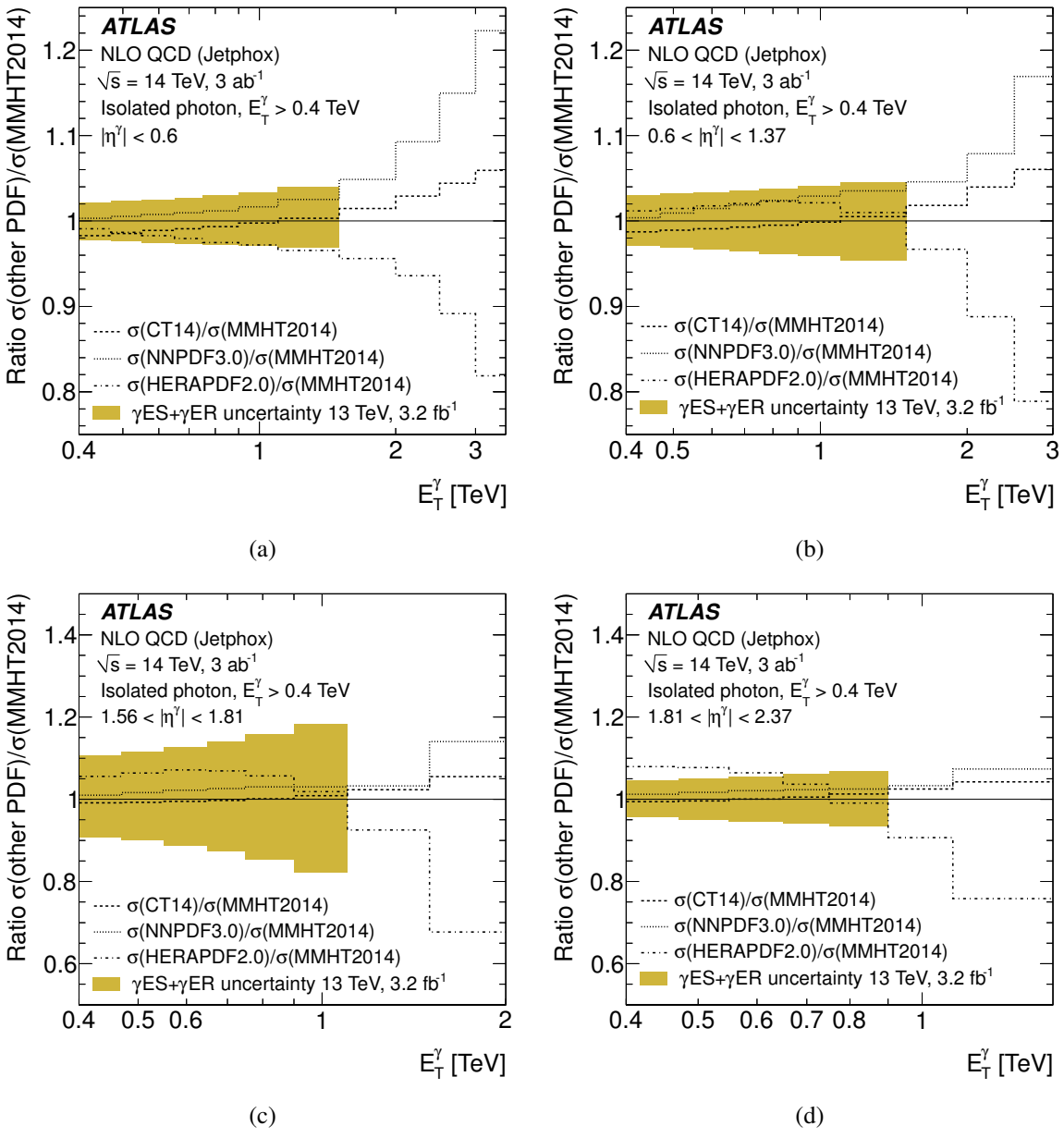

Figure 15: Ratios of the predicted cross sections of inclusive isolated photon events using different PDFs as functions of E_{T}^{γ} in pp collisions at $\sqrt{s}$ = 14 TeV in different ranges of photon pseudorapidity: (a) $|\eta^{\gamma}| < 0.6$, (b) $0.6 < |\eta^{\gamma}| < 1.37$, (c) $1.56 < |\eta^{\gamma}| < 1.81$ and (d) $1.81 < |\eta^{\gamma}| < 2.37$. The ratios of the predictions using CT14 (dashed lines), NNPDF3.0 (dotted lines) and HERAPDF2.0 (dot-dashed lines) over those using MMHT2014 are shown. The shaded band represents the relative systematic uncertainty due to the photon energy scale (γES) and resolution (γER) estimated with 3.2 fb^{-1} of pp collisions at $\sqrt{s}$ = 13 TeV [15].

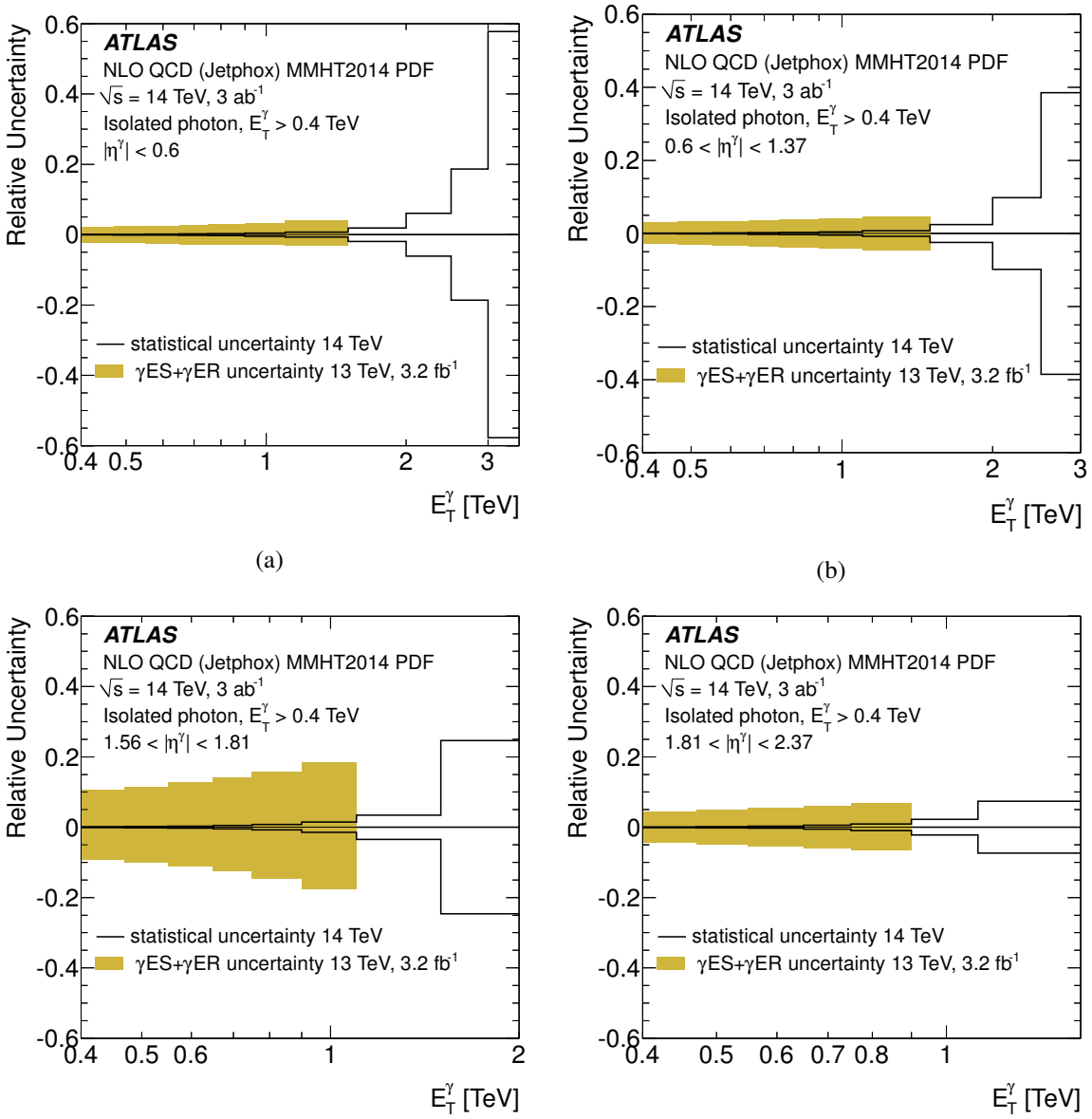

Figure 16: Predicted relative statistical uncertainty on the number of inclusive isolated photon events as a function of E_{T}^{γ} assuming an integrated luminosity of 3 ab^{-1} of pp collision data at $\sqrt{s}$ = 14 TeV in different ranges of photon pseudorapidity: (a) $|\eta^{\gamma}| < 0.6$, (b) $0.6 < |\eta^{\gamma}| < 1.37$, (c) $1.56 < |\eta^{\gamma}| < 1.81$ and (d) $1.81 < |\eta^{\gamma}| < 2.37$. The shaded band represents the relative systematic uncertainty due to the photon energy scale (γES) and resolution (γER) estimated with 3.2 fb^{-1} of pp collisions at $\sqrt{s}$ = 13 TeV [15].

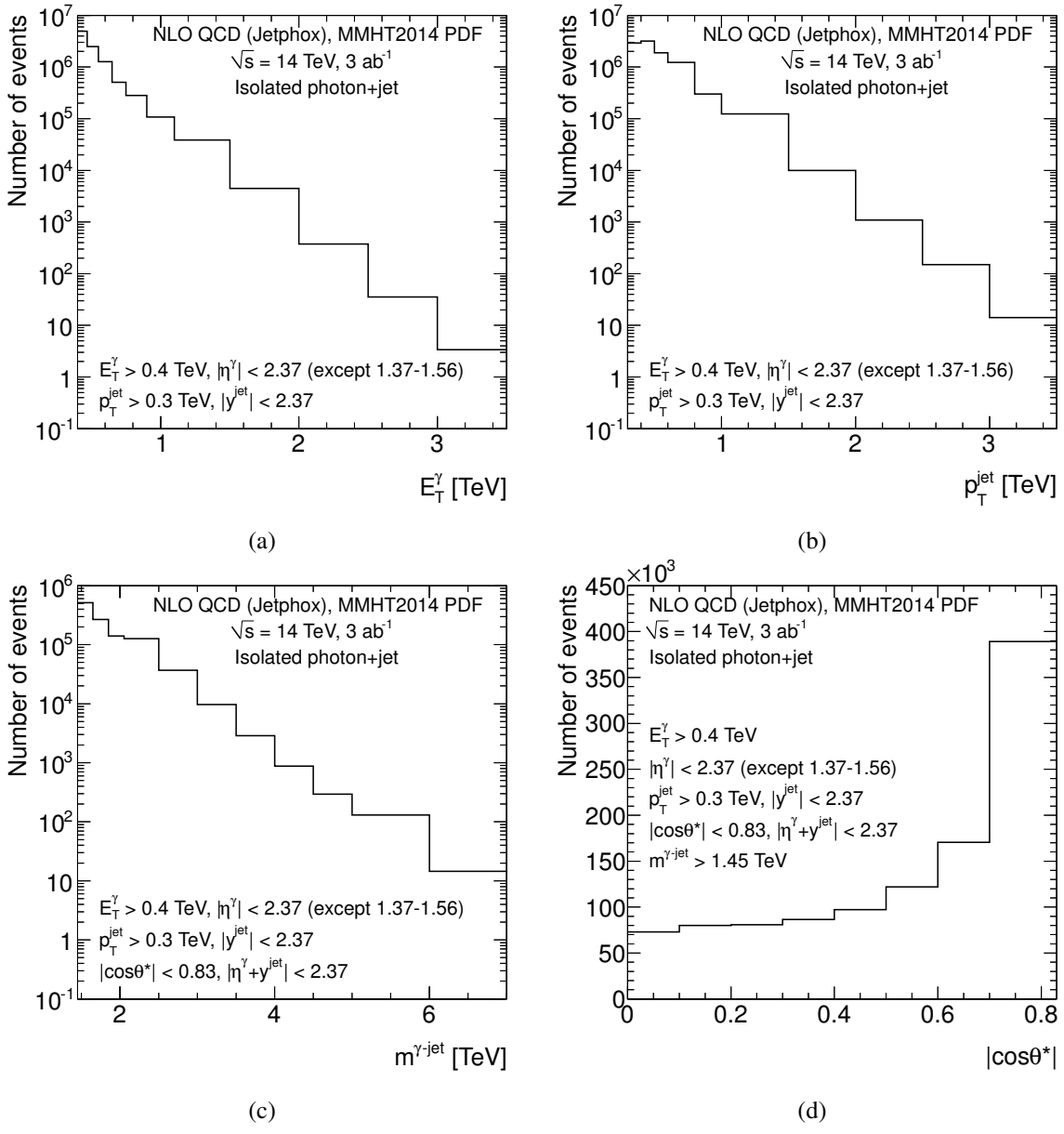

Figure 17: Predicted number of photon+jet events assuming an integrated luminosity of 3 ab^{-1} of collision data at $\sqrt{s}$ = 14 TeV as a function of different observables: (a) E_{T}^{γ}, (b) $p_{\mathrm{T}}^{\mathrm{jet}}$, (c) $m^{\gamma-\mathrm{jet}}$ and (d) $|\cos\theta^{*}|$.

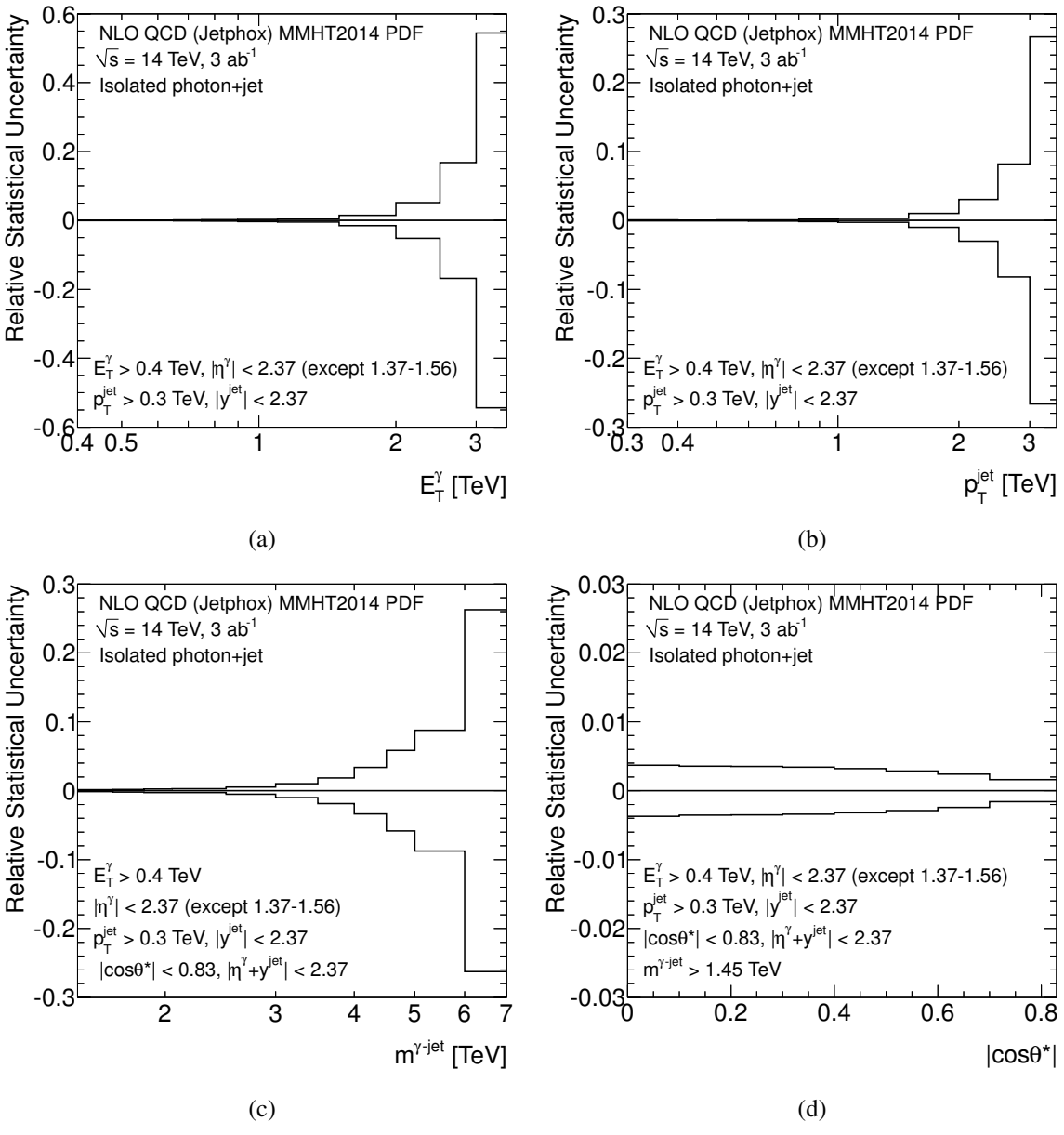

Figure 18: Predicted relative statistical uncertainty on the number of photon+jet events assuming an integrated luminosity of 3 ab^{-1} of pp collision data at $\sqrt{s}$ = 14 TeV as a function of different observables: (a) E_{T}^{γ}, (b) $p_{\mathrm{T}}^{\mathrm{jet}}$, (c) $m^{\gamma-\mathrm{jet}}$ and (d) $|\cos\theta^{*}|$.

4.1.1 Impact of inclusive photon measurements at HL-LHC on the proton PDFs

The impact of the proposed measurements of inclusive isolated photon production in pp collisions at $\sqrt{s} = 14$ TeV in different ranges of $|\eta^\gamma|$ on the proton PDFs is illustrated as follows. The uncertainty in the theoretical predictions due to the uncertainties in the proton PDFs has been evaluated using the studies listed below:

- The MMHT2014 analysis. The uncertainty in the predictions due to the current knowledge of the proton PDFs is estimated by repeating the calculations using the 50 sets from the MMHT2014 error analysis and applying the Hessian method for the evaluation of the PDF uncertainties.
- The Ultimate PDF analysis [39]. This analysis includes the expectations of several measurements at the HL-LHC to quantify their impact on the proton PDFs. It considers measurements of inclusive isolated photon measurements as well as measurements of the production of jets, electroweak gauge bosons and top quark pair production at the HL-LHC. Three scenarios are analysed depending on the assumptions on possible improvements on the experimental systematic uncertainties at HL-LHC. Scenario 1 is conservative, scenario 3 is optimistic and scenario 2 represents an intermediate stage. The resulting profiled PDF sets can be used for phenomenology studies by employing the uncertainty prescription of symmetric Hessian sets, as it is done here.

The relative uncertainty in the predictions due to the uncertainties in the PDFs is shown in Fig. 19 for the MMHT2014 analysis as well as for the three scenarios of the Ultimate PDF analysis. In comparison to the current estimate of the uncertainty using MMHT2014, the measurements at the HL-LHC lead to a significant reduction, which in certain regions such as $E_{\mathrm{T}}^{\gamma} \sim$ 1–2 TeV and $|\eta^\gamma| < 0.6$ is as large as a factor 4.

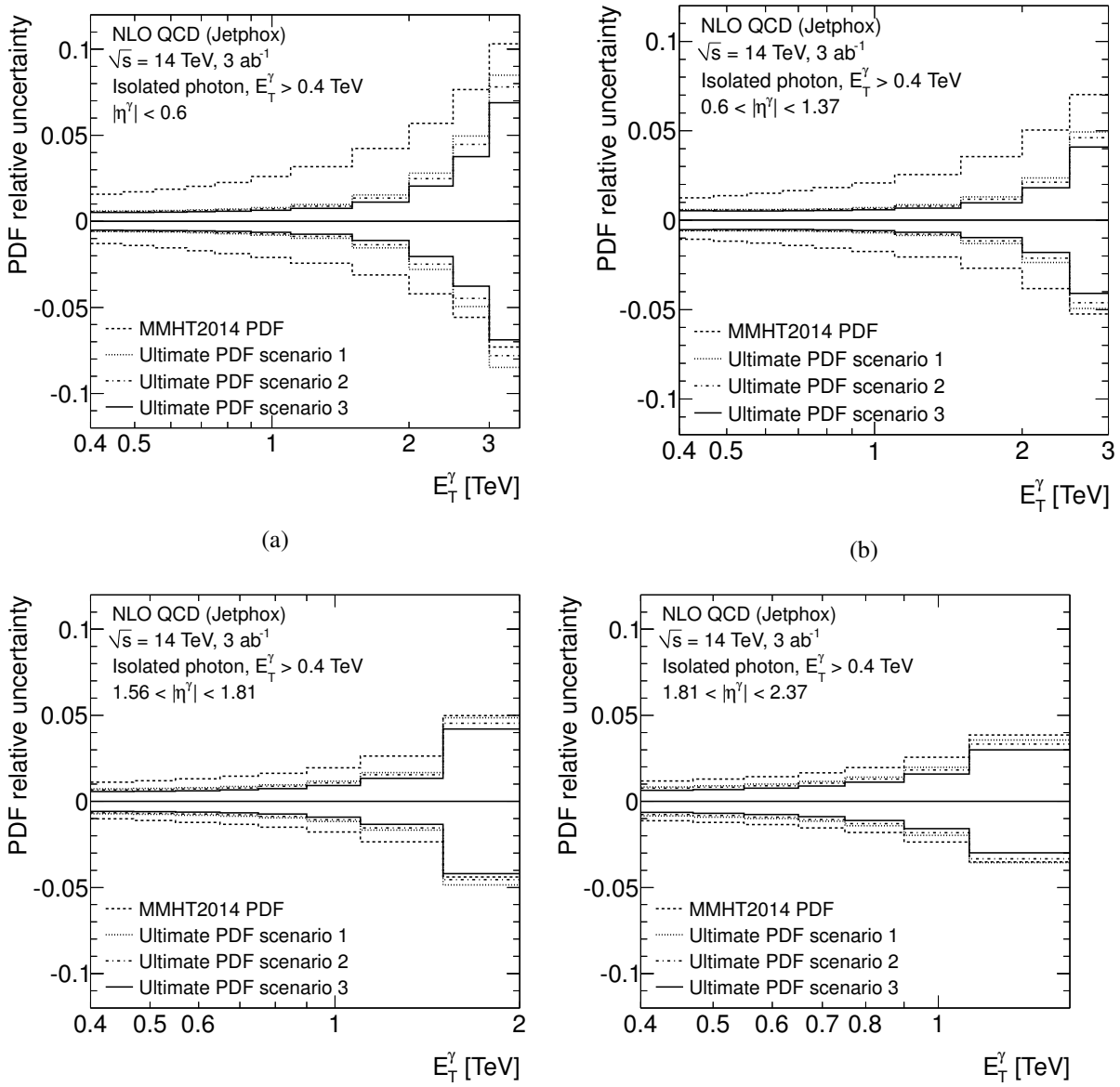

Figure 19: Relative uncertainty in the predicted number of inclusive isolated photon events due to the uncertainties in the PDFs as a function of E_{T}^{γ} in pp collisions at $\sqrt{s} = 14$ TeV in different ranges of photon pseudorapidity: (a) $|\eta^{\gamma}| < 0.6$, (b) $0.6 < |\eta^{\gamma}| < 1.37$, (c) $1.56 < |\eta^{\gamma}| < 1.81$ and (d) $1.81 < |\eta^{\gamma}| < 2.37$. The relative uncertainty due to the PDFs is shown for different PDF sets: the MMHT2014 PDF set (dashed lines) as well as the Ultimate PDF set in scenario 1 (dotted lines), 2 (dot-dashed lines) and 3 (solid lines).

4.1.2 Photon Results at HE-LHC

Prospects are also obtained for inclusive isolated photon and photon+jet production in pp collisions at $\sqrt{s}$ = 27 TeV assuming an integrated luminosity of 15 ab^{-1}. The predicted number of inclusive isolated photon events as a function of E_{T}^{γ} in the different ranges of $|\eta^{\gamma}|$ is shown in Fig. 20. The reach in E_{T}^{γ} is (a) 5 TeV for $|\eta^{\gamma}| < 0.6$ and $0.6 < |\eta^{\gamma}| < 1.37$, (b) 3–3.5 TeV for $1.56 < |\eta^{\gamma}| < 1.81$ and (c) 2.5–3 TeV for $1.81 < |\eta^{\gamma}| < 2.37$. The predicted cross sections are shown in Fig. 21. The ratios of the predictions based on CT14, NNPDF3.0 and HERAPDF2.0 over those using MMHT2014 are shown in Fig. 22 and differences of up to 40% are seen. The predicted relative statistical uncertainty on the number of inclusive isolated photon events as a function of E_{T}^{γ} in different ranges of photon pseudorapidity is shown in Fig. 23. A relative statistical uncertainty below 10% is achieved for photon transverse energies up to (a) 4.5 TeV for $|\eta^{\gamma}| < 0.6$, (b) 4 TeV for $0.6 < |\eta^{\gamma}| < 1.37$, (c) 3 TeV for $1.56 < |\eta^{\gamma}| < 1.81$ and (d) 2.5 TeV for $1.81 < |\eta^{\gamma}| < 2.37$.

The predicted number of photon+jet events as a function of E_{T}^{γ}, $p_{\mathrm{T}}^{\mathrm{jet}}$, $m^{\gamma-\mathrm{jet}}$ and $|\cos\theta^{*}|$ is shown in Fig. 24. The predictions show that the reach in E_{T}^{γ} and $p_{\mathrm{T}}^{\mathrm{jet}}$ is 5 TeV and the reach in $m^{\gamma-\mathrm{jet}}$ is 12 TeV. The predicted relative statistical uncertainty on the number of photon+jet events as a function of the different observables is shown in Fig. 25. The relative statistical uncertainty is below 10% for (a) E_{T}^{γ} up to 4.5 TeV, (b) $p_{\mathrm{T}}^{\mathrm{jet}}$ up to 5 TeV and (c) $m^{\gamma-\mathrm{jet}}$ up to 10 TeV; for $|\cos\theta^{*}|$ the relative statistical uncertainty is below 0.1% for the entire range considered.

4.2 Jet Results

The predicted inclusive jet and dijet cross sections are shown in Figures 26 and 27 in the proton-proton collisions at $\sqrt{s}$ = 14 and 27 TeV, respectively. The cross section values are calculated at NLO pQCD accuracy. The inclusive jet cross sections are calculated as a function of the jet p_{T} in six equal-size bins of absolute jet rapidity for jets in the $|y| < 3$ range with $p_{\mathrm{T}} > 100$ GeV. The dijet cross sections are calculated as a function of the invariant mass of the dijet system (m_{jj}) in six equal-size bins of half absolute rapidity separation between two leading in p_{T} jets.

The predicted number of inclusive jet events as a function of jet p_{T} in the different ranges of the jet rapidity and dijet events as a function of m_{jj} in the pp collisions at $\sqrt{s}$ = 14 and 27 TeV are shown in Fig. 28 and 29. The reach in p_{T} for the inclusive jet cross section measurements is 5.5 TeV in the $|y| < 0.5$ region and 1 TeV in the $2.5 < |y| < 3.0$ region at HL-LHC. For the dijet production the m_{jj} reach is 9 TeV in the $y^{*} < 0.5$ region and 11.5 TeV in the $2.5 < y^{*} < 3.0$ region at HL-LHC. In the case of HE-LHC the inclusive jet cross sections can be measured up to 10 (2.2) TeV in the $|y| < 0.5$ ($2.5 < |y| < 3.0$) region and the dijet production can reach dijet invariant masses of 17 (22) TeV in the $y < 0.5$ ($2.5 < y^{*} < 3.0$) region.

The predicted relative statistical uncertainty in the number of inclusive jet and dijet events as a function of the jet p_{T} in the $|y| < 0.5$ range and m_{jj} in the $y^{*} < 0.5$ bin assuming an integrated luminosity of 3 (15) ab^{-1} of pp collision data at $\sqrt{s}$ = 14 (27) TeV for HL(HE)-LHC is shown in Fig. 30. The relative statistical uncertainty is well below 1% everywhere, except for the highest p_{T} and m_{jj} bins of the measurements.

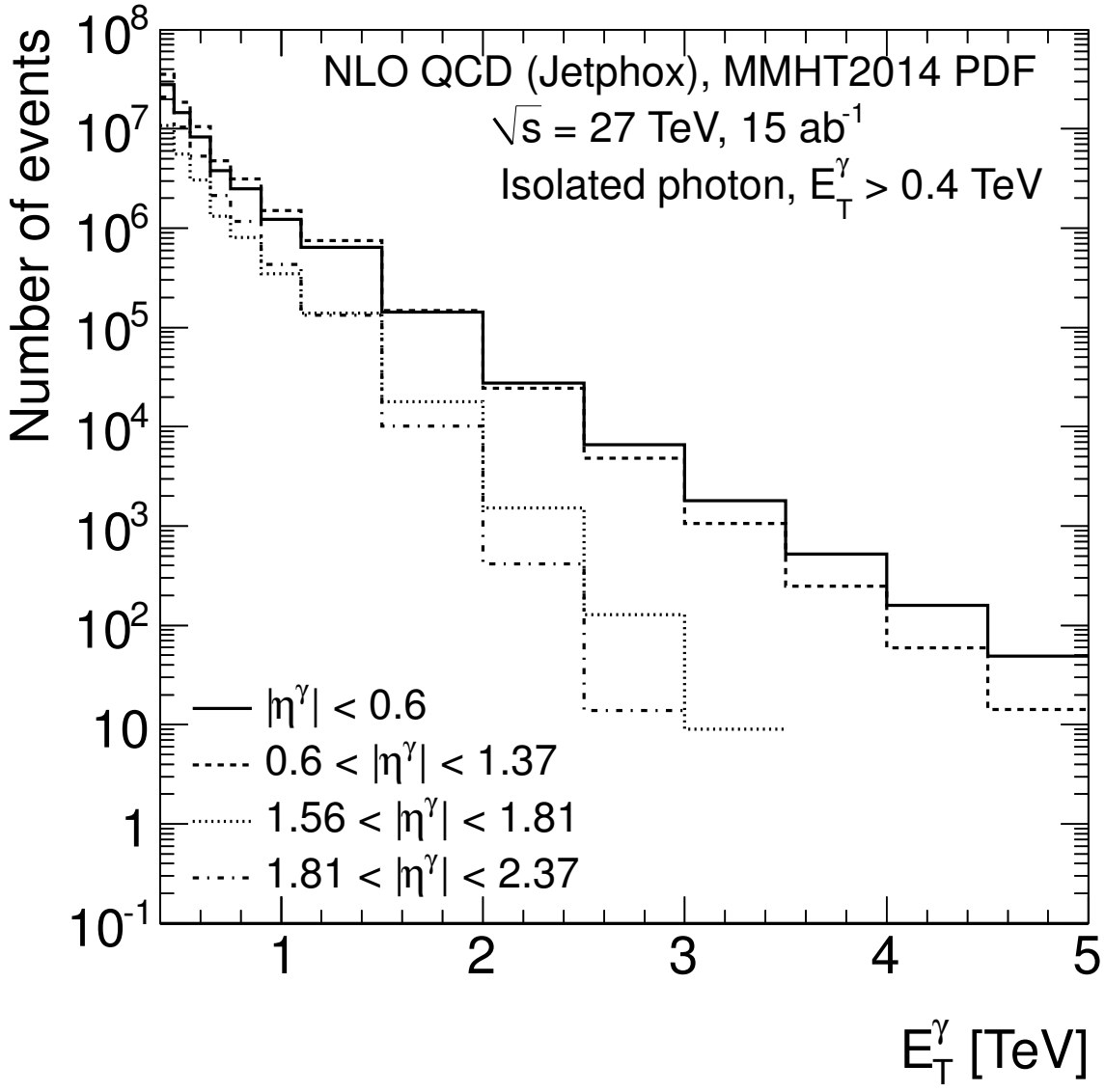

Figure 20: Predicted number of inclusive isolated photon events as a function of E_{T}^{γ} assuming an integrated luminosity of 15 ab^{-1} of pp collision data at $\sqrt{s}$ = 27 TeV in different ranges of photon pseudorapidity: $|\eta^{\gamma}| < 0.6$ (solid histogram), $0.6 < |\eta^{\gamma}| < 1.37$ (dashed histogram), $1.56 < |\eta^{\gamma}| < 1.81$ (dotted histogram) and $1.81 < |\eta^{\gamma}| < 2.37$ (dot-dashed histogram).

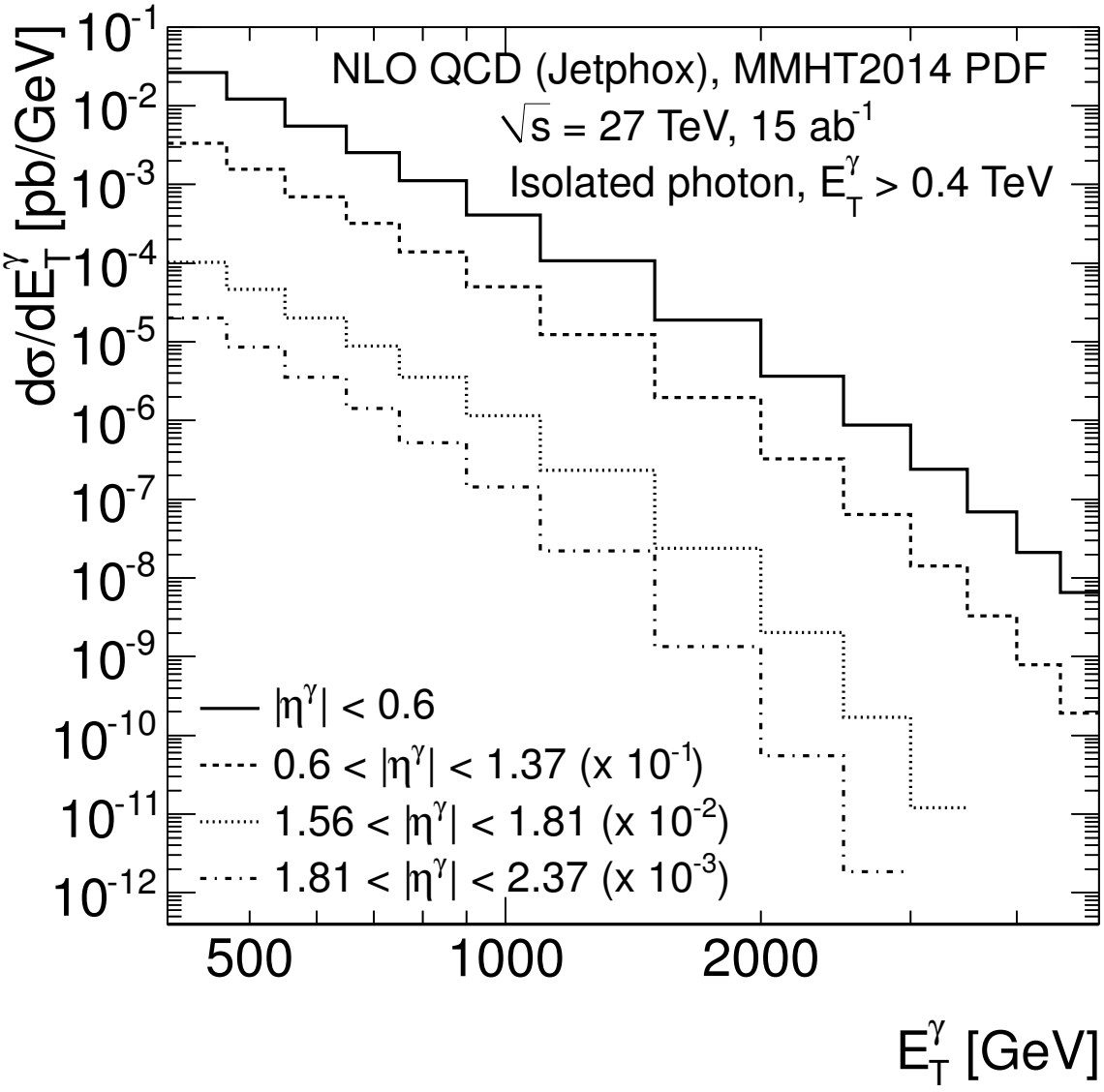

Figure 21: Predicted cross sections in pp collisions at $\sqrt{s}$ = 27 TeV in $|\eta^\gamma| < 0.6$ (solid histogram), $0.6 < |\eta^\gamma| < 1.37$ (dashed histogram), $1.56 < |\eta^\gamma| < 1.81$ (dotted histogram) and $1.81 < |\eta^\gamma| < 2.37$ (dot-dashed histogram).

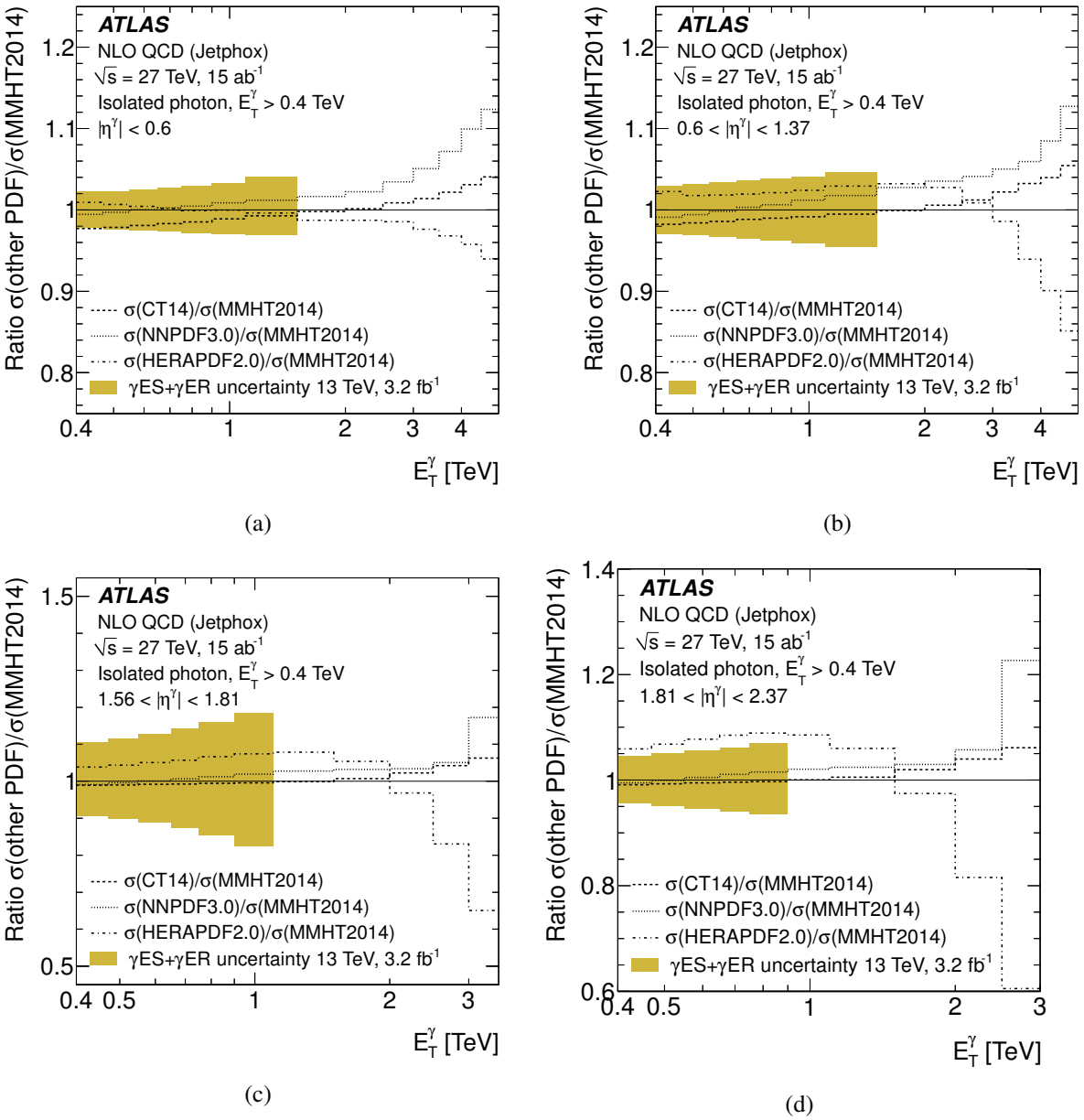

Figure 22: Ratios of the predicted number of inclusive isolated photon events using different PDFs as functions of E_{T}^{γ} in pp collisions at $\sqrt{s}$ = 27 TeV in different ranges of photon pseudorapidity: (a) $|\eta^{\gamma}| < 0.6$, (b) $0.6 < |\eta^{\gamma}| < 1.37$, (c) $1.56 < |\eta^{\gamma}| < 1.81$ and (d) $1.81 < |\eta^{\gamma}| < 2.37$. The ratios of the predictions using CT14 (dashed lines), NNPDF3.0 (dotted lines) and HERAPDF2.0 (dot-dashed lines) over those using MMHT2014 are shown. The shaded band represents the relative systematic uncertainty due to the photon energy scale (γES) and resolution (γER) estimated with 3.2 fb^{-1} of pp collisions at $\sqrt{s}$ = 13 TeV [15].

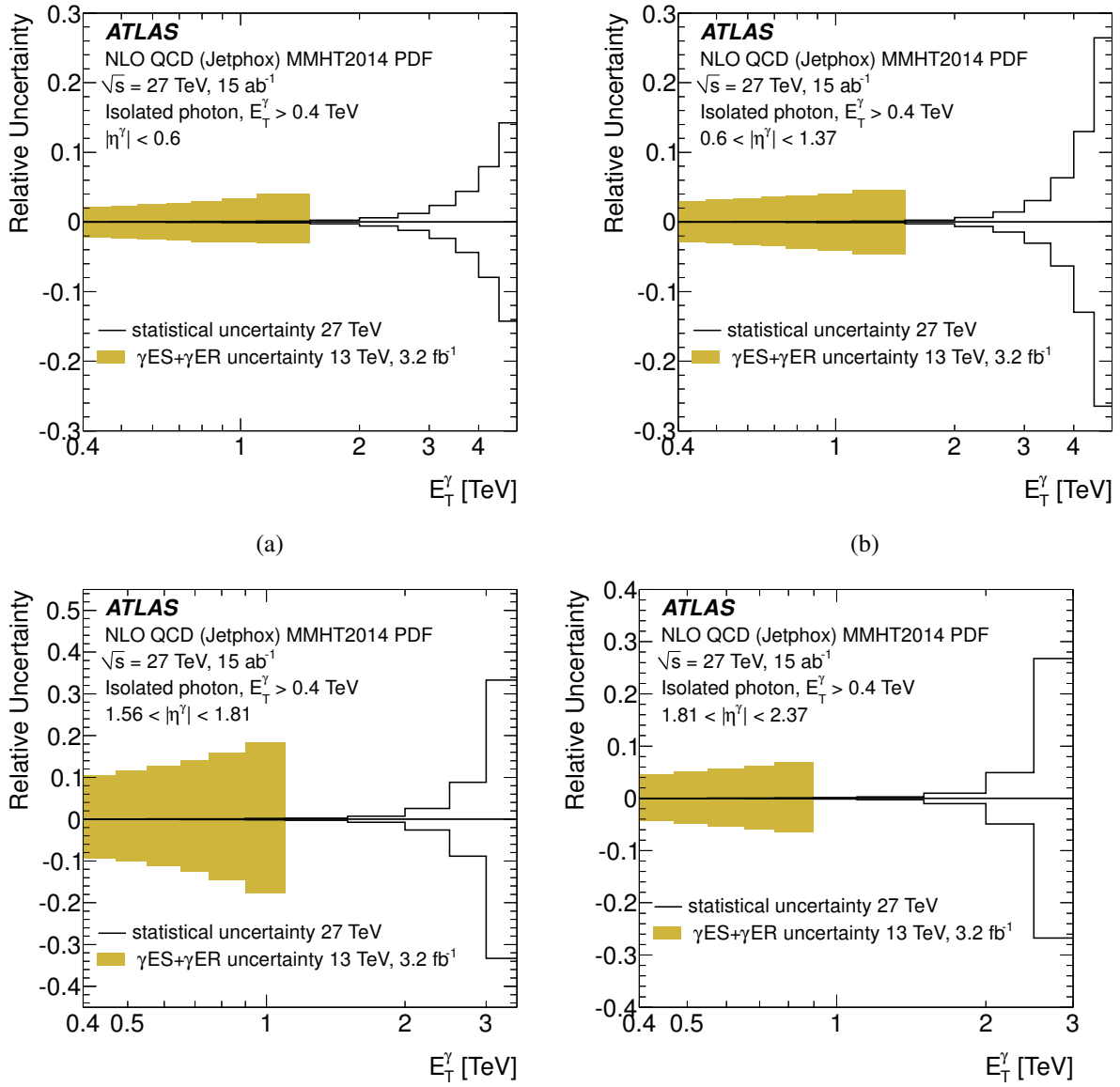

Figure 23: Predicted relative statistical uncertainty on the number of inclusive isolated photon events as a function of E_{T}^{γ} assuming an integrated luminosity of 15 ab^{-1} of pp collision data at $\sqrt{s}$ = 27 TeV in different ranges of photon pseudorapidity: (a) $|\eta^{\gamma}| < 0.6$, (b) $0.6 < |\eta^{\gamma}| < 1.37$, (c) $1.56 < |\eta^{\gamma}| < 1.81$ and (d) $1.81 < |\eta^{\gamma}| < 2.37$. The shaded band represents the relative systematic uncertainty due to the photon energy scale (γES) and resolution (γER) estimated with 3.2 fb^{-1} of pp collisions at $\sqrt{s}$ = 13 TeV [15].

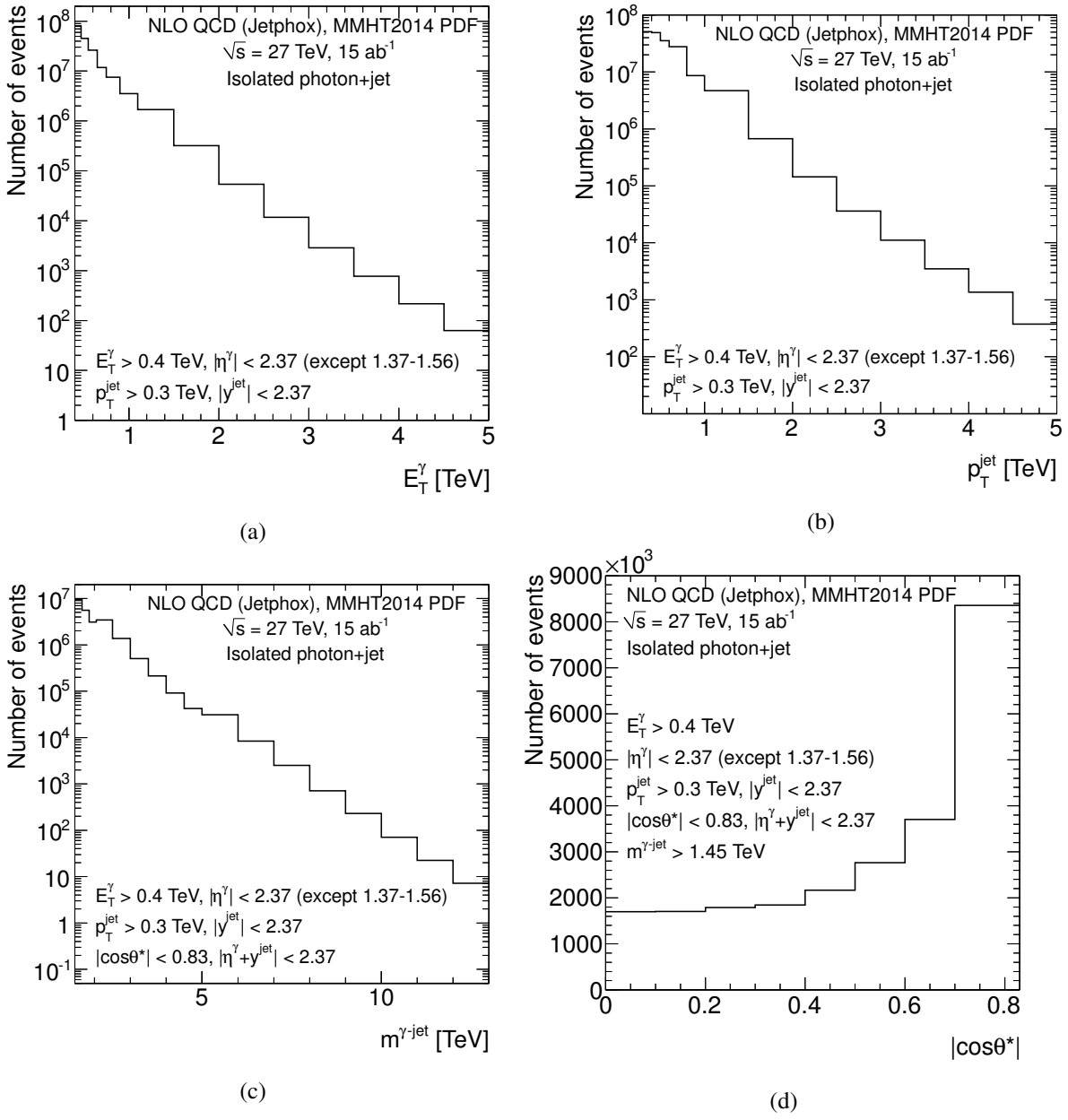

Figure 24: Predicted number of photon+jet events assuming an integrated luminosity of 15 ab^{-1} of pp collision data at $\sqrt{s}$ = 27 TeV as a function of different observables: (a) E_{T}^{γ}, (b) $p_{\mathrm{T}}^{\mathrm{jet}}$, (c) $m^{\gamma-\mathrm{jet}}$ and (d) $|\cos\theta^{*}|$.

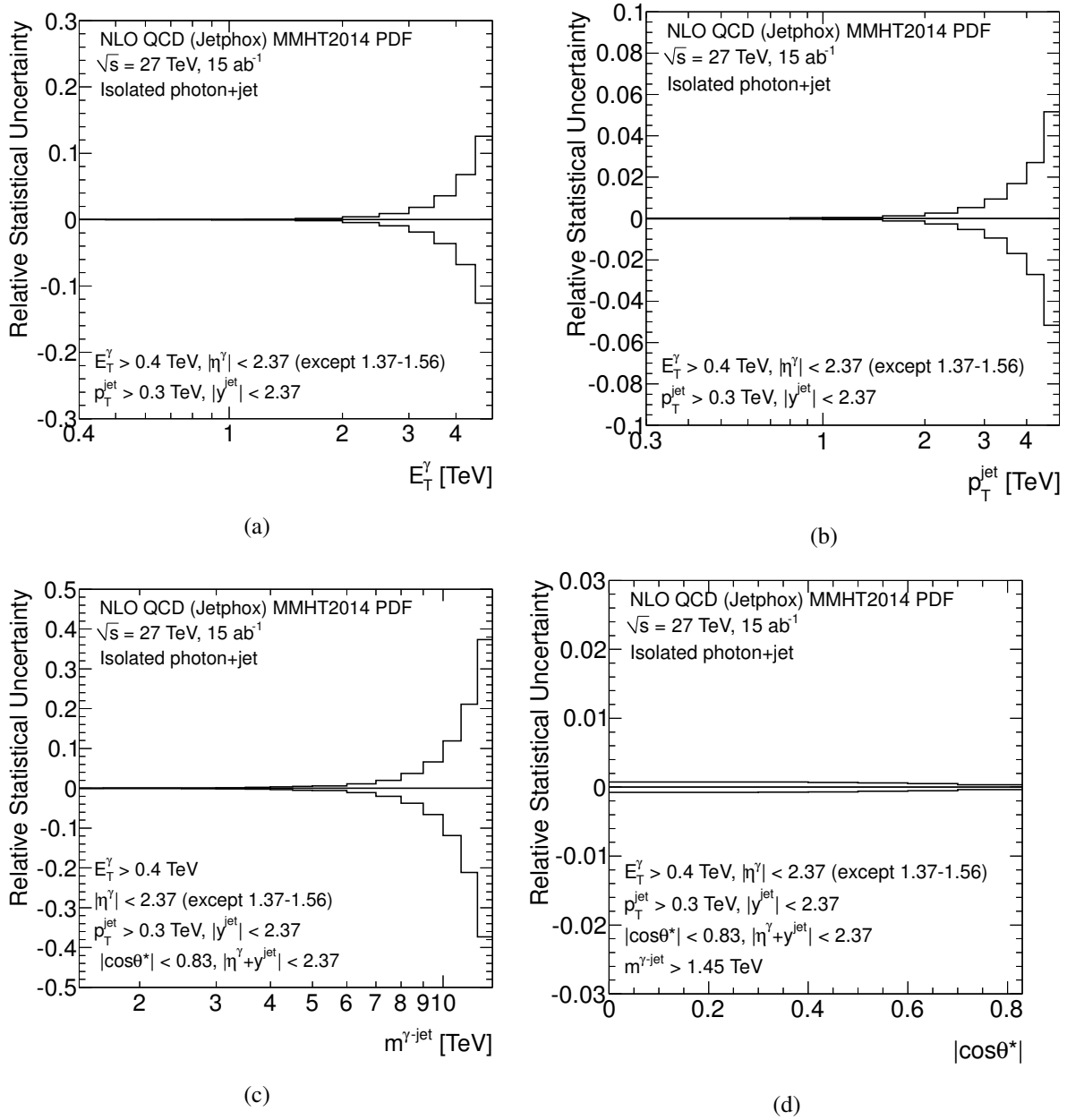

Figure 25: Predicted relative statistical uncertainty on the number of photon+jet events assuming an integrated luminosity of 15 ab^{-1} of pp collision data at $\sqrt{s}$ = 27 TeV as a function of different observables: (a) E_{T}^{γ}, (b) $p_{\mathrm{T}}^{\mathrm{jet}}$, (c) $m^{\gamma-\mathrm{jet}}$ and (d) $|\cos\theta^{*}|$.

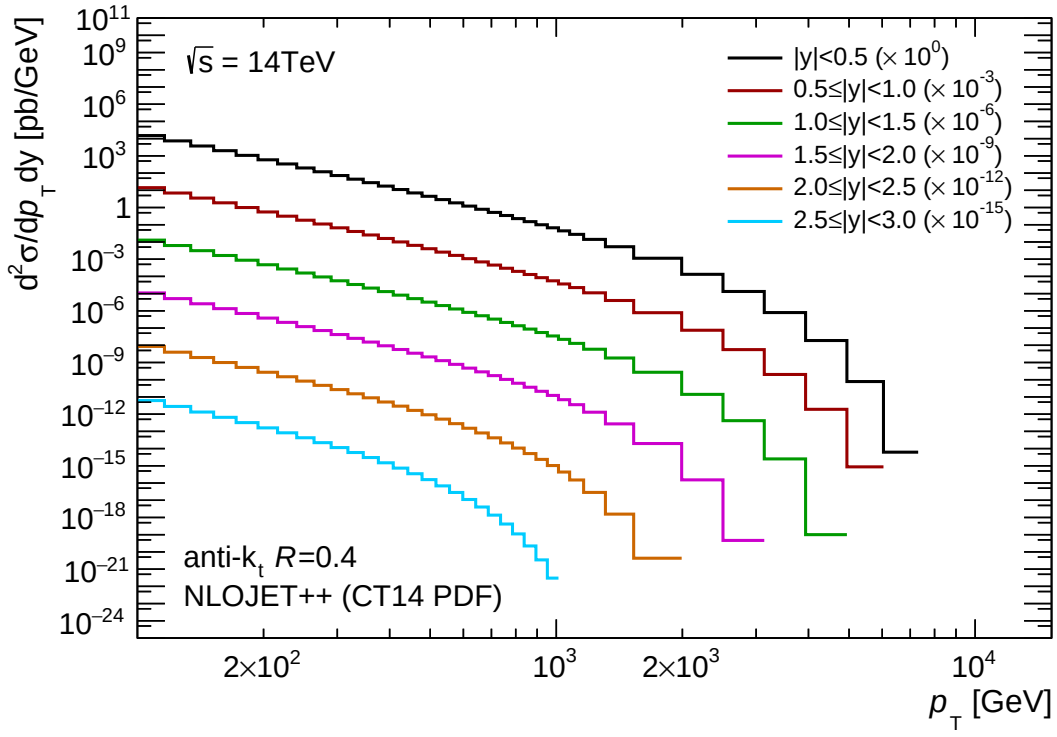

(a) Inclusive jet cross sections

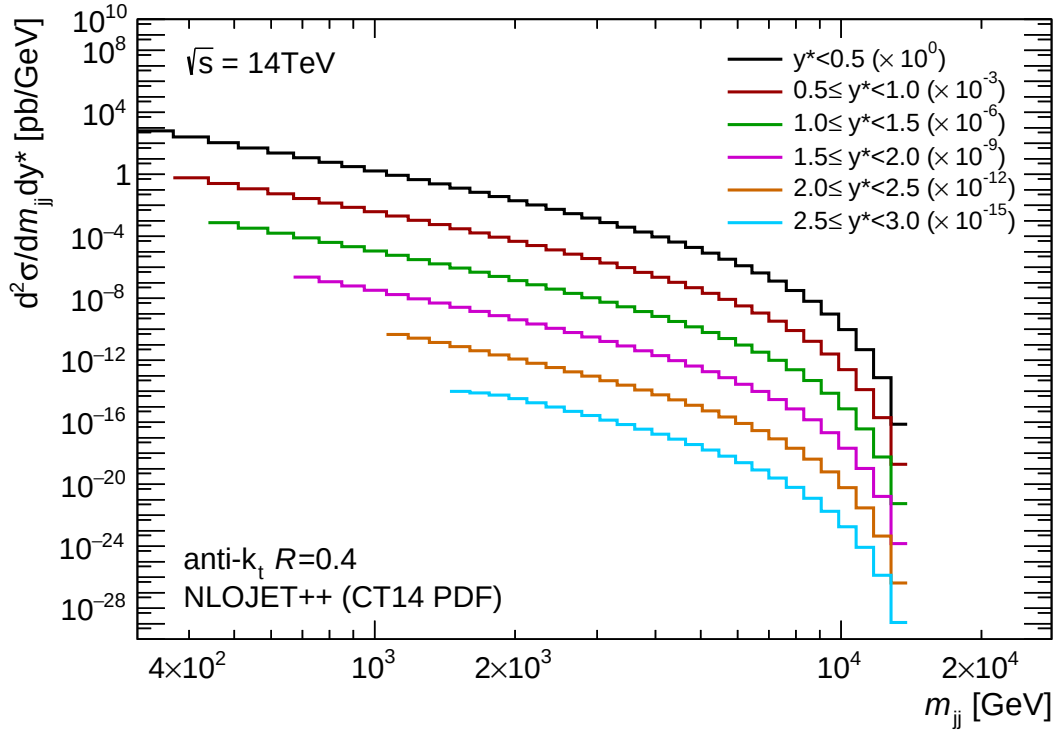

(b) Dijet cross sections

Figure 26: NLO pQCD theory predictions for (a) inclusive jet and (b) dijet cross sections at $\sqrt{s}$ = 14 TeV

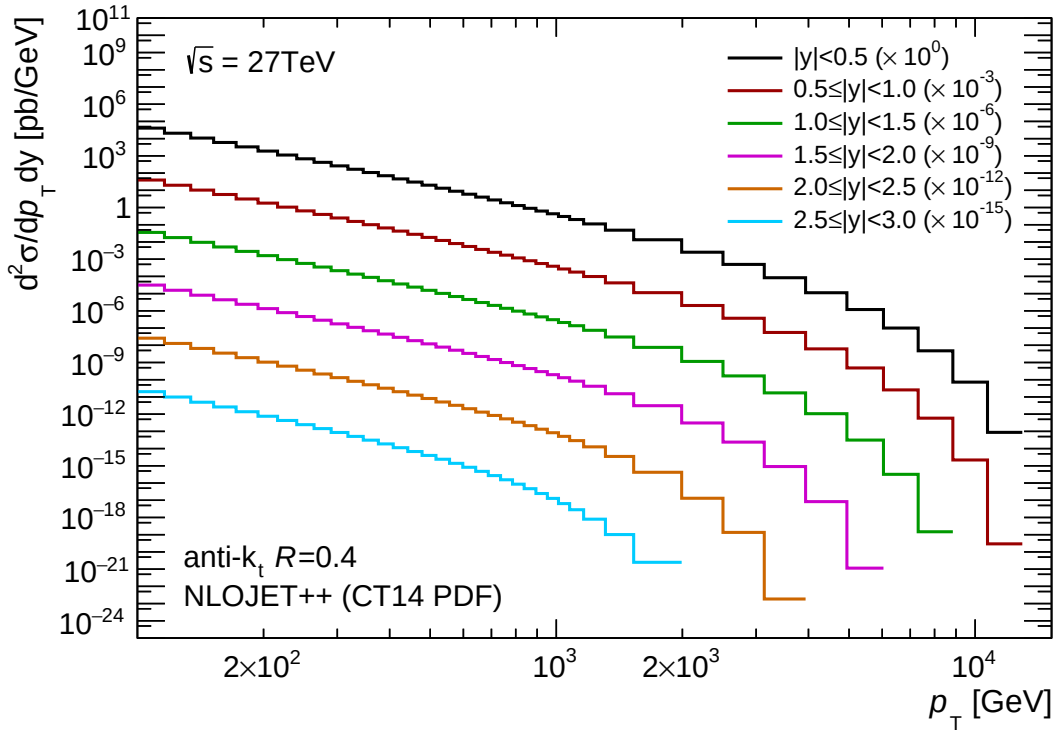

(a) Inclusive jet cross sections

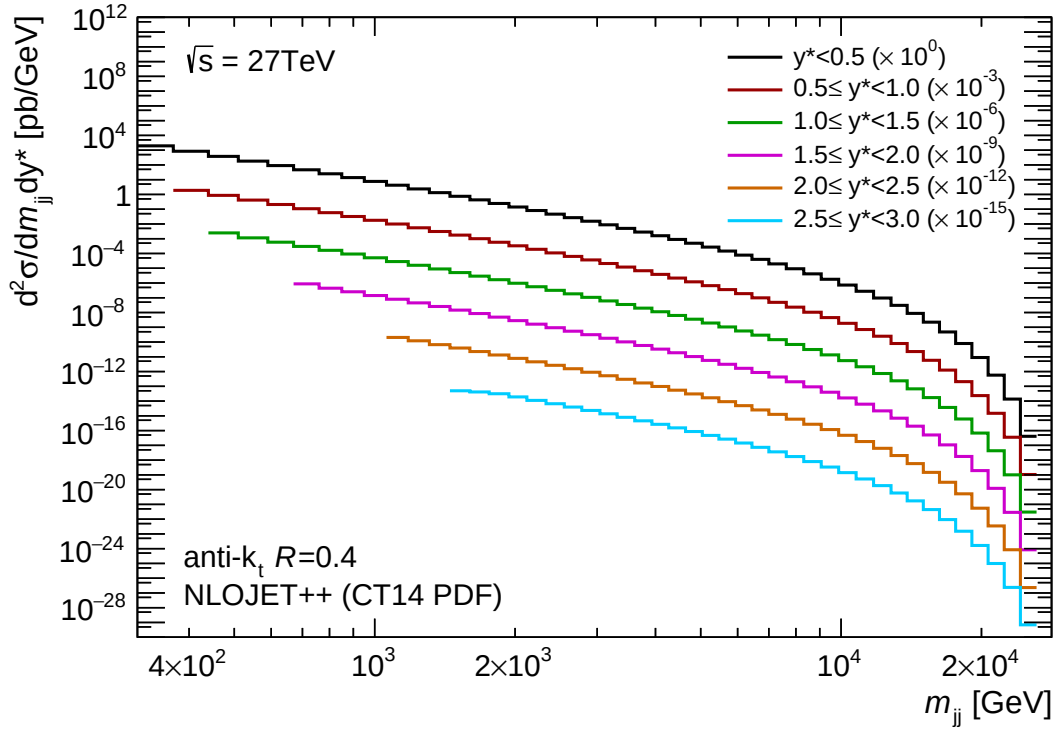

(b) Dijet cross sections

Figure 27: NLO pQCD theory predictions for (a) inclusive jet and (b) dijet cross sections at $\sqrt{s}$ = 27 TeV

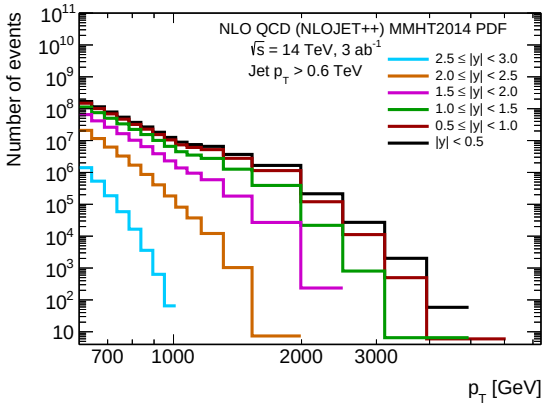

(a) Inclusive jet event yield

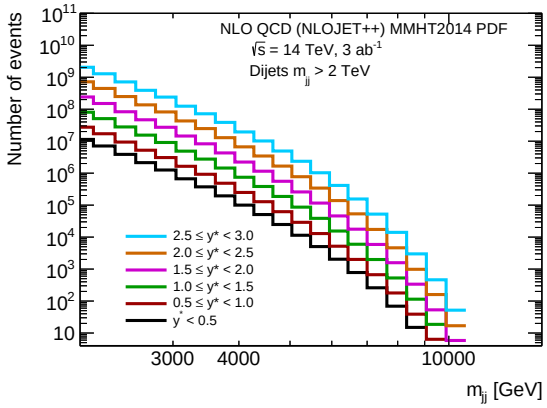

(b) Dijet event yield

Figure 28: Predicted number of inclusive jet and dijet events as a function of jet p_{T} and m_{jj} assuming an integrated luminosity of 3 ab^{-1} of pp collision data at $\sqrt{s} = 14$ TeV in different ranges of $|y|$ and y^*.

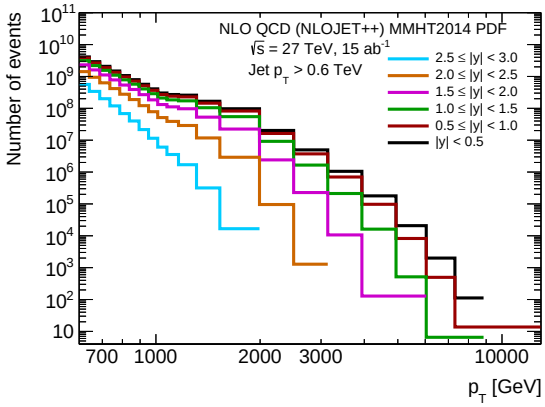

(a) Inclusive jet event yield

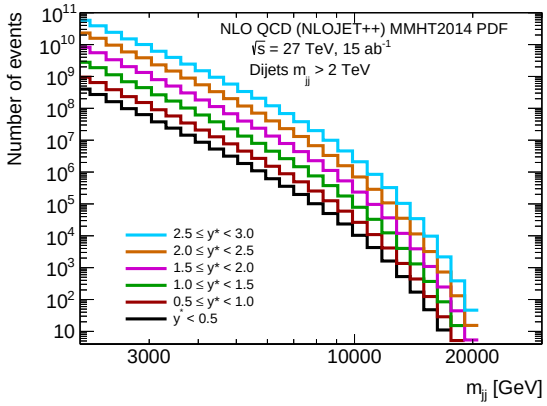

(b) Dijet event yield

Figure 29: Predicted number of inclusive jet and dijet events as a function of jet p_{T} and m_{jj} assuming an integrated luminosity of 15 ab^{-1} of pp collision data at $\sqrt{s} = 27$ TeV in different ranges of $|y|$ and y^*.

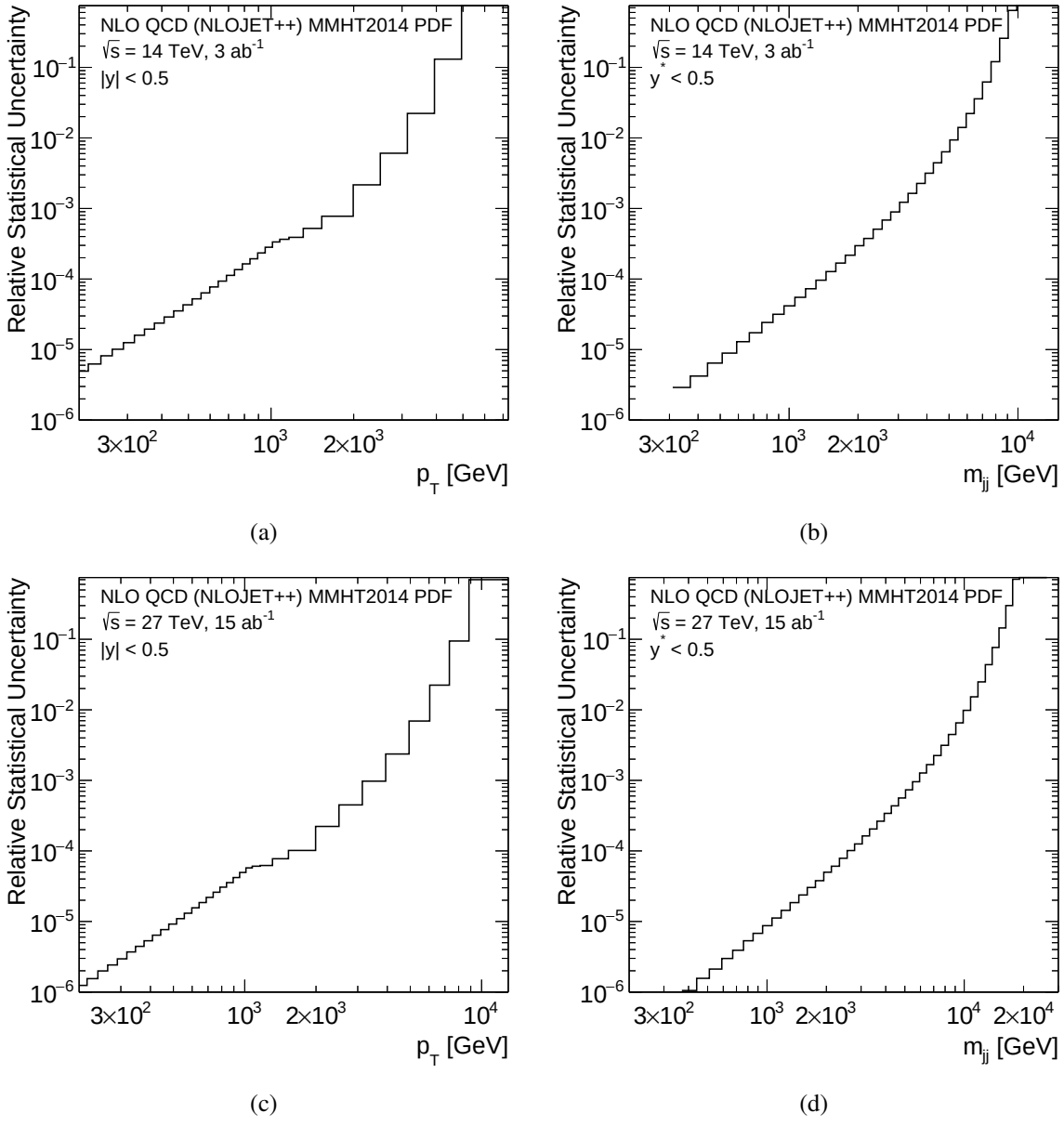

Figure 30: Predicted relative statistical uncertainty in the number of inclusive jet and dijet events as a function of jet p_{T} and m_{jj} assuming an integrated luminosity of 3 (15) ab^{-1} of pp collision data at $\sqrt{s}$ = 14 (27) TeV in $|y| < 0.5$ and $y^{*} < 0.5$ ranges.

The total predicted JES uncertainty in the inclusive jet cross section measurement for the three HL-LHC scenarios is illustrated in Figure 31 and compared to the total JES uncertainty estimate for the Run-2 jet cross section measurements. Total JES uncertainty in the low p_{T} range is same as in Run-2 and is about 2 % lower in the high-p_{T} region. In conservative and pessimistic scenarios JES uncertainties in the cross section are very similar in the intermediate and high-p_{T} range, while JES uncertainty is about 1 % lower in the low-p_{T} range for the optimistic scenario.

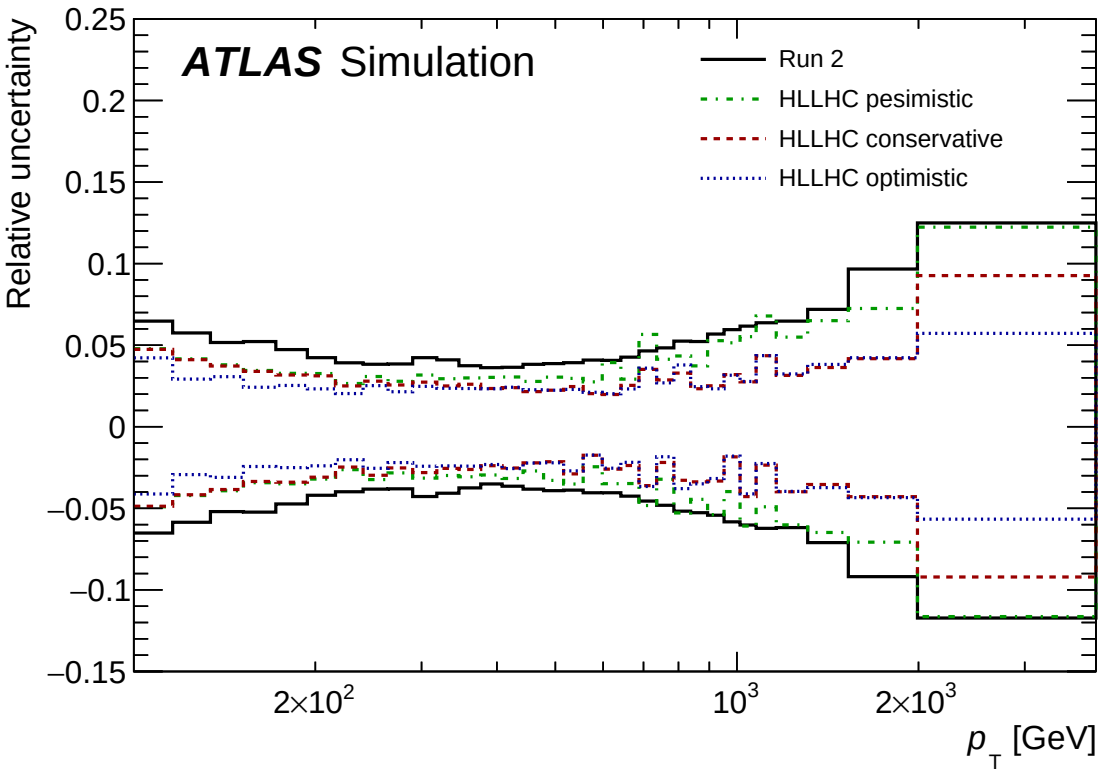

Figure 31: Relative uncertainties in the inclusive jet cross section measurements at the HL-LHC due the JES uncertainties. Three HL-LHC scenarios are compared to the Run-2 performance. Black line corresponds to the Run-2 performance. Green, red and blue lines represent pessimistic, conservative and optimistic scenarios, respectively.

5 Conclusion

Prospects for isolated-photon production inclusively and in association with at least one jet as well as for the inclusive jet and dijet production measurements at the HL-LHC and HE-LHC are presented.

The production of inclusive isolated photons is studied for photon transverse energies above 400 GeV in four ranges of photon pseudorapidity, namely $|\eta^\gamma| < 0.6$, $0.6 < |\eta^\gamma| < 1.37$, $1.56 < |\eta^\gamma| < 1.81$ and $1.81 < |\eta^\gamma| < 2.37$. The reach in E_{T}^{γ} is extended significantly with respect to recent measurements by the ATLAS Collaboration: for the most central region, $|\eta^\gamma| < 0.6$, the E_{T}^{γ} reach is extended from 1.5 TeV to 3–3.5 TeV (5 TeV) assuming an integrated luminosity of 3 ab^{-1} (15 ab^{-1}) of collision data at $\sqrt{s} = 14$ TeV (27 TeV). For photon+jet events, expectations are shown for the distributions in E_{T}^{γ}, $p_{\mathrm{T}}^{\mathrm{jet}}$, $m^{\gamma-\mathrm{jet}}$ and $|\cos\theta^*|$. Jets are required to have $p_{\mathrm{T}}^{\mathrm{jet}} > 300$ GeV and $|y^{\mathrm{jet}}| < 2.37$. An integrated luminosity of 3 ab^{-1} (15 ab^{-1}) of collision data at $\sqrt{s} = 14$ TeV (27 TeV) leads to significant extensions of phase space in comparison with recent measurements at $\sqrt{s} = 13$ TeV: for E_{T}^{γ} and $p_{\mathrm{T}}^{\mathrm{jet}}$ from 1.5 TeV to 3.5 TeV (5 TeV) and for $m^{\gamma-\mathrm{jet}}$ from 3.3 TeV to 7 TeV (12 TeV).

The inclusive jet production cross sections at NLO pQCD accuracy for jets with $p_{\mathrm{T}} > 100$ GeV within $|y| < 3$ in six bins of the absolute jet rapidity are calculated. The non-perturbative effects are taken into account as multiplicative factors. The reach in jet transverse momentum in the central rapidity range in comparison to the recent ATLAS measurements [17] is extended from 3.5 TeV to 5.5 (10) TeV for the inclusive jet p_{T} and from 9 TeV to 11.5 (22) TeV for the dijet invariant mass at the HL-LHC (HE-LHC).

The expected experimental uncertainties in the inclusive jet measurements are studied using three possible scenarios for the precision in the jet energy measurements. In all considered scenarios the inclusive jet cross section measurements will improve compared to Run-2 results precision. In the optimistic scenario, the expected precision will be almost two times better than one in the corresponding Run-2 measurements.

The impact of non-perturbative effects in the high transverse momentum range is small, around 1–2%, allowing to directly test the perturbative QCD predictions at the energy frontiers set by HL/HE-LHC.

A study of PDF sensitivity of the photon and jet production cross sections based on current PDF sets such as MMHT2014, CT14, NNPDF3.0 and HERAPDF2.0 show differences between predictions of up to 30%. That will allow to further constrain the PDFs by performing the photon and jet production measurements at the HL-LHC and HE-LHC. The expected impact on the determination of the proton PDFs of these measurements together with those of other processes such as the production of electroweak gauge bosons and top quark pairs at HL-LHC is illustrated with the estimations of the PDF induced uncertainties based on the PDF4LHC HL-LHC PDF set.

References

[1] L. Evans and P. Bryant, *LHC Machine*, JINST **3** (2008) S08001.

[2] S. D. Ellis, Z. Kunszt and D. E. Soper,
*Two jet production in hadron collisions at order alpha-s**3 in QCD*,
Phys. Rev. Lett. **69** (1992) 1496.

[3] W. T. Giele, E. W. N. Glover and D. A. Kosower,
The Two-Jet Differential Cross Section at $O(\alpha_s^3)$ in Hadron Collisions,
Phys. Rev. Lett. **73** (1994) 2019, arXiv: hep-ph/9403347 [hep-ph].

[4] J. Currie et al., 'Jet cross sections at the LHC with NNLOJET',
14th DESY Workshop on Elementary Particle Physics: Loops and Legs in Quantum Field Theory 2018 (LL2018) St Goar, Germany, April 29-May 4, 2018, 2018, arXiv: 1807.06057 [hep-ph].

[5] J. Currie et al., *N^3LO corrections to jet production in deep inelastic scattering using the Projection-to-Born method*, JHEP **05** (2018) 209, arXiv: 1803.09973 [hep-ph].

[6] J. Currie et al., *Infrared sensitivity of single jet inclusive production at hadron colliders*,
JHEP **10** (2018) 155, arXiv: 1807.03692 [hep-ph].

[7] T. Pietrycki and A. Szczurek, *Photon-jet correlations in pp and pp collisions*,
Phys. Rev. **D 76** (2007) 034003, arXiv: 0704.2158 [hep-ph].

[8] Z. Belghobsi *et al.*, *Photon-jet correlations and constraints on fragmentation functions*,
Phys. Rev. **D 79** (2009) 114024, arXiv: 0903.4834 [hep-ph].

[9] D. d'Enterria and J. Rojo, *Quantitative constraints on the gluon distribution function in the proton from collider isolated-photon data*, Nucl. Phys. **B 860** (2012) 311, and references therein,
arXiv: 1202.1762 [hep-ph].

[10] L. Carminati et al.,
Sensitivity of the LHC isolated-γ+jet data to the parton distribution functions of the proton,
Europhys. Lett. **101** (2013) 61002, arXiv: 1212.5511 [hep-ph].

[11] P. Starovoitov, *Inclusive jet production measured with ATLAS, and constraints on PDFs*,
PoS **DIS2013** (2013) 045.

[12] B. Malaescu, 'Inclusive Jet Production Measured with ATLAS and Constraints on PDFs',
Proceedings, 20th International Workshop on Deep-Inelastic Scattering and Related Subjects (DIS 2012): Bonn, Germany, March 26-30, 2012, 2012 223, arXiv: 1207.4583 [hep-ex].

[13] ATLAS Collaboration, *Search for new phenomena with photon+jet events in proton-proton collisions at $\sqrt{s}$ = 13 TeV with the ATLAS detector*, JHEP **1603** (2016) 041,
arXiv: 1512.05910 [hep-ex].

[14] ATLAS Collaboration, *Search for new phenomena in high-mass final states with a photon and a jet from pp collisions at $\sqrt{s}$ = 13 TeV with the ATLAS detector*, Eur. Phys. J. **C 78** (2018) 102,
arXiv: 1709.10440 [hep-ex].

[15] ATLAS Collaboration, *Measurement of the cross section for inclusive isolated-photon production in pp collisions at $\sqrt{s}$ = 13 TeV using the ATLAS detector*, Phys. Lett. **B 770** (2017) 473,
arXiv: 1701.06882 [hep-ex].

[16] ATLAS Collaboration, *Measurement of the cross section for isolated-photon plus jet production in pp collisions at $\sqrt{s}$ = 13 TeV using the ATLAS detector*, Phys. Lett. **B 780** (2018) 578,
arXiv: 1801.00112 [hep-ex].

[17] ATLAS Collaboration, *Measurement of inclusive jet and dijet cross-sections in proton-proton collisions at $\sqrt{s}$ = 13 TeV with the ATLAS detector*, JHEP **05** (2018) 195,
arXiv: 1711.02692 [hep-ex].

[18] ATLAS Collaboration, *The ATLAS Experiment at the CERN Large Hadron Collider*,
JINST **3** (2008) S08003.

[19] ATLAS Collaboration, *Technical Design Report for the ATLAS Inner Tracker Strip Detector*, tech. rep. CERN-LHCC-2017-005. ATLAS-TDR-025, CERN, 2017, URL: http://cds.cern.ch/record/2257755.

[20] ATLAS Collaboration, *Technical Design Report for the ATLAS Inner Tracker Pixel Detector*, tech. rep. CERN-LHCC-2017-021. ATLAS-TDR-030, CERN, 2017, URL: http://cds.cern.ch/record/2285585.

[21] ATLAS Collaboration, *Technical Design Report for the Phase-II Upgrade of the ATLAS Muon Spectrometer*, tech. rep. CERN-LHCC-2017-017. ATLAS-TDR-026, CERN, 2017, URL: http://cds.cern.ch/record/2285580.

[22] ATLAS Collaboration, *Technical Proposal: A High-Granularity Timing Detector for the ATLAS Phase-II Upgrade*, tech. rep. CERN-LHCC-2018-023. LHCC-P-012, CERN, 2018, URL: http://cds.cern.ch/record/2623663.

[23] ATLAS Collaboration, *Technical Design Report for the Phase-II Upgrade of the ATLAS LAr Calorimeter*, tech. rep. CERN-LHCC-2017-018. ATLAS-TDR-027, CERN, 2017, URL: http://cds.cern.ch/record/2285582.

[24] ATLAS Collaboration, *Technical Design Report for the Phase-II Upgrade of the ATLAS Tile Calorimeter*, tech. rep. CERN-LHCC-2017-019. ATLAS-TDR-028, CERN, 2017, URL: http://cds.cern.ch/record/2285583.

[25] ATLAS Collaboration, *Technical Design Report for the Phase-II Upgrade of the ATLAS TDAQ System*, tech. rep. CERN-LHCC-2017-020. ATLAS-TDR-029, CERN, 2017, URL: http://cds.cern.ch/record/2285584.

[26] ATLAS Collaboration, *Expected performance for an upgraded ATLAS detector at High-Luminosity LHC*, tech. rep. ATL-PHYS-PUB-2016-026, CERN, 2016, URL: https://cds.cern.ch/record/2223839.

[27] R. Assmann et al., *First Thoughts on a Higher-Energy LHC*, tech. rep. CERN-ATS-2010-177, CERN, 2010, URL: https://cds.cern.ch/record/1284326.

[28] J. Abelleira et al., *High-Energy LHC design*, Journal of Physics: Conference Series **1067** (2018) 022009, URL: http://stacks.iop.org/1742-6596/1067/i=2/a=022009.

[29] M. Cacciari, G. Salam and G. Soyez, *The anti-k_t jet clustering algorithm*, JHEP **04** (2008) 063, arXiv: 0802.1189 [hep-ex].

[30] ATLAS Collaboration, *Dynamics of isolated-photon plus jet production in pp collisions at $\sqrt{s} = 7$ TeV with the ATLAS detector*, Nucl. Phys. **B 875** (2013) 483, arXiv: 1307.6795 [hep-ex].

[31] ATLAS Collaboration, *High-E_T isolated-photon plus jets production in pp collisions at $\sqrt{s} = 8$ TeV with the ATLAS detector*, Nucl. Phys. **B 918** (2017) 257, arXiv: 1611.06586 [hep-ex].

[32] S. Catani, M. Fontannaz, J. Ph. Guillet and E. Pilon,
Cross section of isolated prompt photons in hadron-hadron collisions, JHEP **0205** (2002) 028, arXiv: hep-ph/0204023.

[33] P. Aurenche, M. Fontannaz, J. Ph. Guillet, E. Pilon and M. Werlen,
A new critical study of photon production in hadronic collisions,
Phys. Rev. **D 73** (2006) 094007, and references therein, arXiv: hep-ph/0602133.

[34] L. A. Harland-Lang, A. D. Martin, P. Motylinski and R. S. Thorne,
Parton distributions in the LHC era: MMHT 2014 PDFs, Eur. Phys. J. **C 75** (2015) 204, arXiv: 1412.3989 [hep-ph].

[35] L. Bourhis, M. Fontannaz and J.Ph. Guillet,
Quark and gluon fragmentation functions into photons, Eur. Phys. J. **C 2** (1998) 529, arXiv: hep-ph/9704447.

[36] S. Dulat et al.,
New parton distribution functions from a global analysis of quantum chromodynamics,
Phys. Rev. **D 93** (2016) 033006, arXiv: 1506.07443 [hep-ph].

[37] H1 and ZEUS Collaborations, H. Abramowicz *et al.*, *Combination of measurements of inclusive deep inelastic $e^{\pm}p$ scattering cross sections and QCD analysis of HERA data*,
Eur. Phys. J. **C 75** (2015) 580, arXiv: 1506.06042 [hep-ex].

[38] NNPDF Collaboration, R.D. Ball *et al.*, *Parton distributions for the LHC Run II*,
JHEP **1504** (2015) 040, arXiv: 1410.8849 [hep-ph].

[39] R. A. Khalek, S. Bailey, J. Gao, L. Harland-Lang and J. Rojo,
Towards Ultimate Parton Distributions at the High-Luminosity LHC, (2018),
arXiv: 1810.03639 [hep-ph].

[40] M. Cacciari, G. P. Salam and G. Soyez, *FastJet User Manual*, EPJC **72** (2012) 1896,
arXiv: 1111.6097 [hep-ph].

[41] ATLAS Collaboration, *Jet energy scale measurements and their systematic uncertainties in proton–proton collisions at $\sqrt{s}$ = 13 TeV with the ATLAS detector*,
Phys. Rev. **D 96** (2017) 072002, arXiv: 1703.09665 [hep-ex].

[42] ATLAS Collaboration, *Performance of pile-up mitigation techniques for jets in pp collisions at $\sqrt{s}$ = 8 TeV using the ATLAS detector*, Eur. Phys. J. **C 76** (2016) 581,
arXiv: 1510.03823 [hep-ex].

[43] ATLAS Collaboration, *Jet global sequential corrections with the ATLAS detector in proton-proton collisions at sqrt(s) = 8 TeV*, tech. rep. ATLAS-CONF-2015-002, CERN, 2015,
URL: https://cds.cern.ch/record/2001682.

[44] ATLAS Collaboration,
A measurement of the calorimeter response to single hadrons and determination of the jet energy scale uncertainty using LHC Run-1 pp-collision data with the ATLAS detector,
Eur. Phys. J. **C 77** (2017) 26, arXiv: 1607.08842 [hep-ex].

[45] J. M. Campbell and R. K. Ellis, *An Update on vector boson pair production at hadron colliders*,
Phys. Rev. **D 60** (1999) 113006, arXiv: hep-ph/9905386 [hep-ph].

[46] T. Carli et al., *A posteriori inclusion of parton density functions in NLO QCD final-state calculations at hadron colliders: The APPLGRID Project*, Eur. Phys. J. **C 66** (2010) 503,
arXiv: 0911.2985 [hep-ph].

[47] A. Buckley et al., *LHAPDF6: parton density access in the LHC precision era*, Eur. Phys.l J. **C 75** (2015) 132, ISSN: 1434-6052, URL: https://doi.org/10.1140/epjc/s10052-015-3318-8.

[48] J. Butterworth et al., *PDF4LHC recommendations for LHC Run II*, J. Phys. **G 43** (2016) 023001, arXiv: 1510.03865 [hep-ph].

[49] ATLAS Collaboration, *Measurement of the inclusive $W^{\pm}$ and Z/gamma cross sections in the electron and muon decay channels in pp collisions at $\sqrt{s}$ = 7 TeV with the ATLAS detector*, Phys. Rev. **D 85** (2012) 072004, arXiv: 1109.5141 [hep-ex].

[50] ATLAS Collaboration, *Measurement of the cross section for top-quark pair production in pp collisions at $\sqrt{s}$ = 7 TeV with the ATLAS detector using final states with two high-pt leptons*, JHEP **05** (2012) 059, arXiv: 1202.4892 [hep-ex].

[51] ATLAS Collaboration, *Measurement of inclusive jet and dijet production in pp collisions at $\sqrt{s}$ = 7 TeV using the ATLAS detector*, Phys. Rev. **D 86** (2012) 014022, arXiv: 1112.6297 [hep-ex].

[52] R. D. Ball et al., *Parton distributions from high-precision collider data*, Eur. Phys. J. **C 77** (2017) 663, arXiv: 1706.00428 [hep-ph].

[53] S. Alekhin, J. Blümlein, S. Moch and R. Placakyte, *Parton distribution functions, α_s, and heavy-quark masses for LHC Run II*, Phys. Rev. **D 96** (2017) 014011, arXiv: 1701.05838 [hep-ph].

[54] T. Sjöstrand et al., *An Introduction to PYTHIA 8.2*, Comput. Phys. Commun. **191** (2015) 159, arXiv: 1410.3012 [hep-ph].

[55] ATLAS Collaboration, *Summary of ATLAS Pythia 8 tunes*, ATL-PHYS-PUB-2012-003, 2012, URL: http://cds.cern.ch/record/1474107.

[56] S. Dittmaier, A. Huss and C. Speckner, *Weak radiative corrections to dijet production at hadron colliders*, JHEP **11** (2012) 095, arXiv: 1210.0438 [hep-ph].